PERSPECTIVE

Spin-crossover in iron(II)-Schiff base complexes

Kuppusamy Senthil Kumar, [ID] *[a] Yosef Bayeh, [ID] [b] Tesfay Gebretsadik, [ID] [b] Fikre Elemo, [ID] [b] Mamo Gebrezgiabher, [ID] [b] Madhu Thomas [ID] *[b] and Mario Ruben [ID] *[a,c]

The spin-crossover (SCO) phenomenon is one of the most prominent examples of bi-stability in molecular chemistry, and the SCO complexes are proposed for nanotechnological applications such as memory units, sensors, and displays. Since the discovery of the SCO phenomenon in tris(N,N-dialkyl-dithiocarbamato)iron(III) complexes, numerous investigations have been made to obtain bi-stable SCO complexes undergoing spin-state switching at or around room temperature (RT). Valiant efforts have also been made to elucidate the structure–property relationship in SCO complexes to understand the factors—such as ligand-field strength, molecular geometry, and intermolecular interactions—governing the SCO. Schiff base ligands are an important class of nitrogen-rich chelating ligands used to prepare SCO complexes, because the Schiff base ligands are easy to synthesize and tailor with additional functionalities. Iron(II)-Schiff base SCO complexes are a well-studied class of SCO active complexes due to the propensity of the complexes to undergo bi-stable SCO. In this context, this perspective attempts to elucidate the structure–SCO property relationships governing SCO in selected mono-, bi-, and multi-nuclear iron(II)-Schiff base complexes.

1. Introduction

1.1. General introduction to spin-crossover (SCO)

Spin-crossover is a reversible transition between low-spin (LS) and high-spin (HS) states mediated by external stimuli: examples include temperature, light, pressure, and electric field.[1–16] The LS to HS switching or *vice versa* causes changes in the magnetic moment of the SCO complexes; some of the SCO complexes also show thermochromism.[17–20] Temperature is the most commonly used stimulus to induce SCO at the bulk scale. Light is employed as a stimulus to effect LS to HS switching at low-temperatures ($T < 10$ K), which is termed light-induced excited spin-state trapping (LIESST). Note, a reverse-LIESST is also possible, that is, HS to LS switching.[21–28] Pressure is a unique stimulus applied to cause SCO in bulk samples,[29,30] whereas an electric field is used to switch spin-states at the single molecule level, for example, an SCO complex embedded in a molecular junction or surface bound thin SCO films.[31,32]

SCO could be observed for a transition metal complex with a $3d^n$ ($n = 4$–7) electronic configuration. The SCO is most commonly encountered in $3d^6$ octahedral or pseudo-octahedral iron(II) complexes featuring ligands of moderate field-strength. Note, the LS and HS state of an SCO active iron(II) complex is diamagnetic and paramagnetic, respectively. Depending on the ligand field splitting (Δ_o) and the pairing energy (P), there are two ways that electrons can populate in the t_{2g} and e_g set of orbitals of an iron(II) complex (Fig. 1(top)). For strong field ligands $\Delta_o > P$, hence a LS state is preferred due to the paring of electrons in the t_{2g} set of orbitals. In the case of weak field ligands $\Delta_o < P$ and a HS state are favoured. For an intermediate field strength $\Delta_o = P$ and it is possible to induce the SCO by the application of an external stimulus as mentioned before.[33]

SCO in molecular complexes is classified as: (a) gradual (b) abrupt (c) hysteretic (d) stepwise, and (d) incomplete (Fig. 1 (bottom)).[4] Much interest has been focused on SCO complexes exhibiting the cooperative first-order spin-state switching with hysteresis, and such complexes are termed bi-stable complexes,[3,10,12,18,34–38] because the complexes can exist in two different stable electronic states depending on the history.[39] Bi-stable SCO complexes showing a relatively large thermal hysteresis ($\Delta T \geq 45$ K) centered around room temperature (RT) are desired for applications, especially to obtain molecule-based switching and memory devices.[12]

Factors such as the ligand-field strength, counter anions, co-crystallized lattice solvent molecules, and intermolecular interactions influence the SCO properties, especially the SCO

[a]Institut de Physique et de Chimie des Matériaux-Université de Strasbourg23, Rue du Loess, BP 43, F-67034 Strasbourg, France.
E-mail: senthil.kuppusamy@ipcms.unistra.fr
[b]Department of Industrial Chemistry, Addis Ababa Science and Technology University, P. O. Box. 16417, Addis Ababa, Ethiopia.
E-mail: madhu.thomas@aastu.edu.et
[c]Institute of Nanotechnology, Karlsruhe Institute of Technology, PF 3640, D-76021 Karlsruhe, Germany. E-mail: mario.ruben@kit.edu
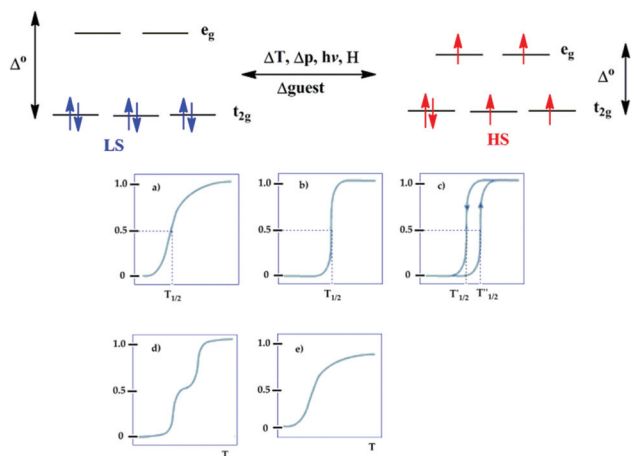
Fig. 1 (top) Crystal field splitting of an iron(ɪɪ) complex in its LS and HS states and (bottom) various types of SCO behaviour: (a) gradual, (b) abrupt, (c) with hysteresis, (d) two-step transition (plateau), and (e) incomplete.

Chart 1 (a) General synthesis route for Schiff base ligands; R could be an alkyl or aryl functionality and (b) some examples of Schiff base ligands with different denticity used to prepare iron(ɪɪ) SCO complexes.

temperature $T_{1/2}$ ($T_{1/2}$ is a temperature where equal proportions of LS and HS states exist), steepness/abruptness of the curve (that is, the $\chi_M T$ *versus* T plot, where χ_M = molar magnetic susceptibility and T = temperature), and thermal hysteresis width (ΔT).[2] The abruptness of solid SCO complexes depends on the nature of cooperative interactions between the switching units, that is, on the efficiency of the crystal lattice to transmit the geometry changes and electronic spin-state change that occur during the spin transition.[40,41] Most SCO-active iron(ɪɪ) complexes are mono-nuclear,[34,38,42–44] and reports on the discrete bi- or multi-nuclear iron(ɪɪ)-complexes are relatively rare.[45,46] Schiff base ligands are versatile platforms to produce mono-, bi-, and multi-nuclear iron(ɪɪ)-SCO complexes with remarkable properties such as abrupt, hysteretic, and RT spin-state switching.[37,45–48]

1.2. Schiff base ligand systems

Schiff bases are condensation products of primary amines and carbonyl compounds.[49] Structurally, a Schiff base (also known as an imine or azomethine) is an analogue of a ketone or aldehyde in which the carbonyl group (–C═O) is converted by a primary amine into an imine or azomethine (–HC═N–) functionality (Chart 1).

Schiff bases can be of different denticity (Chart 1) capable of forming stable complexes with transition metals and hence are an important and well-studied class of ligands.[49–56] Schiff bases can only act as chelating ligands if they bear another group capable of metal coordination, usually the hydroxyl, sufficiently near the site of condensation in such a way that a five- or six-membered chelate ring can be formed when coordinating with a metal ion. Schiff bases behave as flexi-dentate ligands and commonly coordinate through the oxygen and nitrogen atoms of the deprotonated phenolic and azomethine groups, respectively. This class of ligands plays an important role in the formation of metal complexes that show photo- and thermochromism in the solid state by proton transfer from the
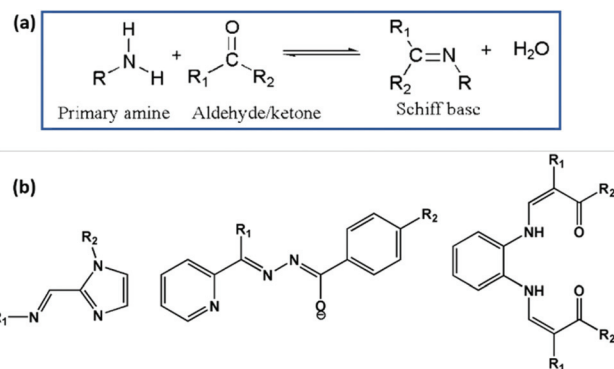
hydroxyl (–OH) to the imine (–C═N–) functionality. An N_6-coordination environment around the central metal ion is the most commonly employed coordination mode to prepare SCO complexes. Schiff base ligands can form the desired N_6-iron(ɪɪ) complexes along with N_4O_2-iron(ɪɪ) complexes. Remarkably, some of the N_4O_2-iron(ɪɪ) Schiff base complexes are reported to show abrupt and hysteretic RT SCO as discussed in the following sections.[47,57] By tailoring the Schiff-base ligands with appropriate functional groups, the SCO behaviour of the iron(ɪɪ) complexes can be tuned. Usually, a range of precursor aldehydes and amines featuring desired functional groups are used to synthesize and design Schiff base ligands.[57]

This possibility of synthesizing Schiff base ligands tailored with functional entities such as luminescent[58,59] and self-assembly[60,61] directing groups is an added advantage towards the realization of application oriented multifunctional SCO materials. The following sections will focus on factors governing SCO in mono-, bi- and multi-nuclear iron(ɪɪ)-Schiff base SCO complexes.

2. SCO in mononuclear iron(ɪɪ)-Schiff base complexes

2.1. [FeN₄O₂] complexes composed of tetradentate Jäger-type N₂O₂²⁻ and imidazole/N-heterocyclic ligands

Detailed structure–SCO property relationships in iron(ɪɪ) complexes composed of Schiff base-like ligands and imidazole have been reported by Weber and co-workers.[34,62] Two different modifications of a mixed ligand iron(ɪɪ)-complex— [FeL1(HIm)₂](1)—were synthesized by treating the precursor Schiff base complex—[FeL1(MeOH)₂]—with an excess of HIm in MeOH (Scheme 1). During the reaction, two of the MeOH molecules from the precursor complex were replaced by the imidazole ligands leading to the formation of 1. The precipitation of 1 from the boiling reaction mixture yielded 1^{HT}, which exhibited a 70 K thermal hysteresis width. Powder or microcrystalline forms of another modification of 1—1^{LT}—was obtained by cooling the reaction mixture and allowing it to

R_1 = COOEt, R_2 = Me: **L1**
R_1 = COOMe, R_2 = Me: **L2**
R_1 = COOEt, R_2 = Ph: **L3**
R_1 = COPh, R_2 = Me: **L4**
R_1 = COMe, R_2 = Me: **L5**

$[Fe(L1)(HIm)_2]$ **(1)**
$[Fe(L2)(HIm)_2]$ **(2)**
$[Fe(L3)(HIm)_2]$ **(3)**
$[Fe(L4)(HIm)_2]$ **(4)**

$[Fe(L5)(HIm)]$ **(5)**
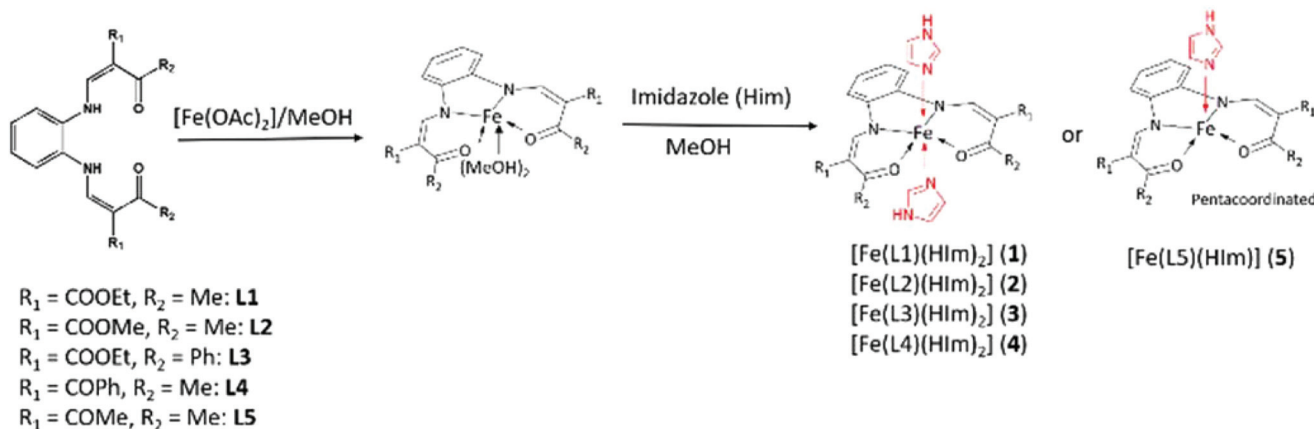
Scheme 1 Synthesis of charge-neutral $[FeN_4O_2]$ complexes **1–5**.

stand at RT or 4 °C. Crystallographic analyses of 1^{HT} and 1^{LT} revealed a distorted octahedral coordination geometry around iron(II) with equatorially and axially coordinated tetradentate **L1** and imidazole ligands, respectively.

Both 1^{HT} and 1^{LT} showed first order SCO with thermal hysteresis (bi-stable SCO). A 70 K wide thermal hysteresis loop with $T_{1/2}$ = 279 K was reported for 1^{HT}, whereas, 1^{LT} showed above RT SCO with $T_{1/2}$ = 329 K and ΔT = 5 K as depicted in Fig. 2.

Two different intermolecular hydrogen-bonding interactions between the neighbouring complex moieties constituted a 2D network structure in the crystal lattice of 1^{HT} as shown in Fig. 2a. On the other hand, a 3D network structure composed of three different H-bonding interactions was observed in the crystal lattice of 1^{LT}, see Fig. 2b. These intermolecular hydrogen-bonding interactions caused abrupt SCO by mediating cooperative interactions between the switching entities and contributed to the opening of the hysteresis loop upon LS to HS switching or *vice versa*.
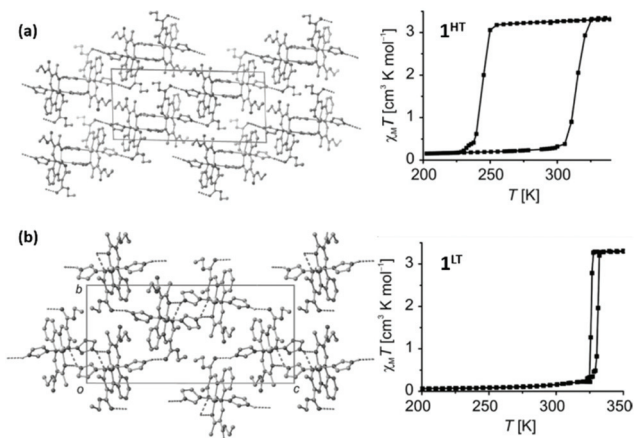
Fig. 2 (a) 2D-self-organization of 1^{HT} and the corresponding $\chi_M T$ versus T plot and (b) 3D-self-organization of 1^{LT} and the corresponding $\chi_M T$ versus T plot.

The observation of hydrogen bonding interaction mediated bistable SCO in **1** prompted the synthesis of structurally similar $[FeLn(Him)_2]$, n = 2–5 complexes (Scheme 1). Attempts were made to obtain the complexes by substituting the methanol molecules of the precursor complex, $[FeLn(MeOH)_2]$ (n = 2–5), by imidazole. The product of the complex formation reaction is highly influenced by the nature of the solvent, concentration of the precursor complex, and the ratio of the iron(II) complex to imidazole.[63]

Successful syntheses of hexacoordinate $[FeLn(Him)_2]$ (n = 2–5), complexes were not realized in all cases. For **L5**, only penta-coordinate complex **5** was obtained; the use of a large excess of imidazole and various solvents as the reaction medium failed to push the equilibrium more towards the desired hexa-coordinated complex. Remarkably, octahedral complexes with the composition $[FeLn(Him)_2]$ (**L2** (**2**), **L3** (**3**), and **L4** (**4**)), were obtained for the three remaining ligands **L2**–**L4**. The spin-state switching characteristics of the powder complexes depend on the precipitation temperature. Complexes **2** and **3** showed gradual SCO with $T_{1/2}$ = 344 K and $T_{1/2}$ = 170 K, respectively. For **3**, the coexistence of equal proportions of LS and HS iron(II) states was observed at 37 K indicating incomplete SCO.

To probe the role of the extended π-system and N-heterocycles of varying structures in tuning the SCO behaviour, a family of iron(II) complexes (Fig. 3) featuring equatorially coordinated tetradentate diaminonaphthalene-based Schiff base-like ligands and axially coordinated N-heterocycle ligands were synthesized.[64] Complex **6** (**L6**: R = Ph, L^{ax} = Py) crystalized with a pyridine solvent and showed a stable and reversible first-order SCO ($T_{1/2}$ = 175 K) with a small hysteresis as depicted in Fig. 3b.

Complex **7** (**L7**: R = OMe, L^{ax} = Py) also contained a lattice pyridine molecule. The complex showed a gradual and two-step SCO with $T_{1/2}^1$ = 150 K and $T_{1/2}^2$ = 80 K; the SCO is incomplete with a residual HS fraction of 0.29 at 60 K ($\chi_M T$ = 0.84 cm^3 $kmol^{-1}$). Annealing of the complex at 400 K led to the loss of pyridine from the lattice as indicated by thermo-
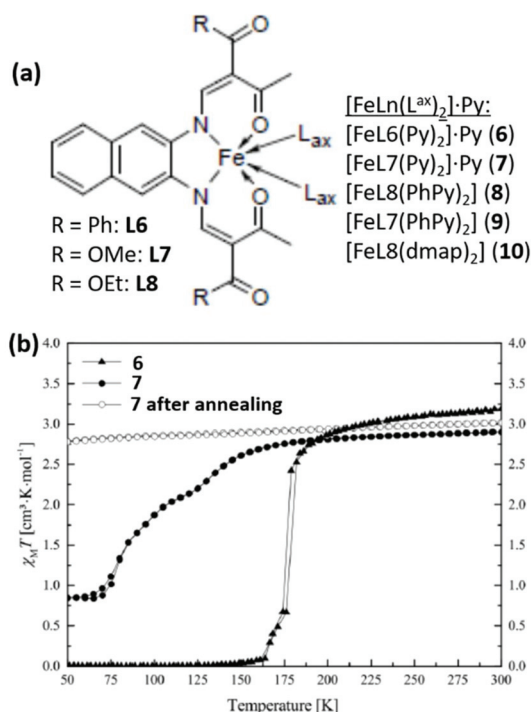
Fig. 3 Structure of diaminonapthalene-based iron(II) complexes **6–10** and (b) $\chi_M T$ versus T plots of **6** and **7**. Reprinted with permission from ref. 34 and 62. Copyright (2008 and 2011) John Wiley and Sons.

gravimetric analysis (TGA): the desolvated **7** remained HS throughout the investigated 300 K to 50 K temperature range as shown in Fig. 3(b). Thus, lattice-solvent dependence of SCO in **7** is demonstrated. Remarkably, complexes **8** (**L8**: R = COOEt, L^{ax} = PhPy) and **9** (**L7**: R = OMe, L^{ax} = PhPy) showed abrupt SCO in both cooling and warming modes and exhibited a hysteresis loop of about 10 K. Complex **10** (**L8**: R = COOEt, L^{ax} = dmap) showed stable two-step SCO with the first gradual step starting at 273 K and ending at 189 K ($T^1_{1/2}$ = 224 K); the second abrupt SCO-step occurred with $T^2_{1/2}$ = 149 K.

Cooperative SCO behaviour mediated by lipid bilayer like self-assembly is demonstrated in a family of amphiphilic SCO complexes composed of equatorially coordinated Schiff base like ligands tethered with alkyl chains and axially coordinated N-heterocycle ligands.[65–67]

In brief, first order SCO with or without hysteresis and step-wise spin-state switching behaviour are observed in [FeN₄O₂] type complexes (**1–10**) composed of Schiff base like ligands—**L1–L8**—and a range of axially coordinated heterocycles. The nature and occurrence of SCO in the complexes is governed by preparation conditions, intermolecular interactions, and the presence or absence of lattice solvent molecules.

2.2. [FeN₄O₂] complexes composed of tridentate N₂O⁻ ligands

Tridentate pyridylmethylene-aminophenol (pap: **L9**) quinolyl-salicylaldimine (qsal: **L10–L15**), and quinolyl-napthaldimine (qnal: **L16** and **L17**) ligand systems featuring a N₂O⁻ donor set (Chart 2) were used to prepare charge-neutral iron(II) com-
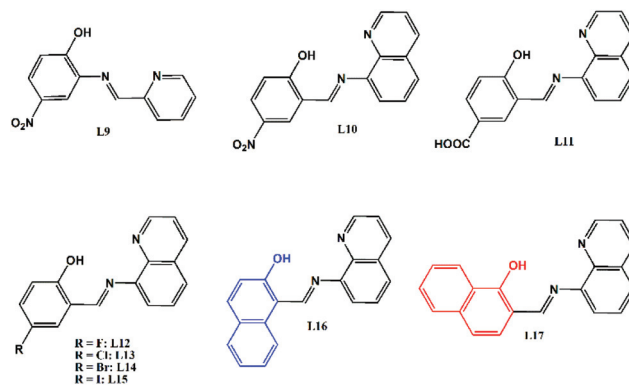
Chart 2 Structures of pap, qsal, and, qnal ligands used to prepare iron (II)-SCO complexes.

plexes. The absence of anions in the lattice of charge-neutral complexes may allow the switching entities to have larger interactions, which in turn could facilitate cooperative spin-state switching.

The role of intermolecular elastic and electrostatic interactions contributing to the occurrence of cooperative spin-state switching is demonstrated for the charge-neutral [Fe(L9)₂] complex (**11**). The complex showed an abrupt SCO around RT with $T_{1/2}$ = 299 K and ΔT = 17 K as depicted in Fig. 4(a). The complex is also LIESST active, and T_{LIESST} = 58 K was reported. In the crystal lattice of **11**, hydrogen-bonding interactions among the molecules formed infinite chains, which are interconnected *via* a 3D-network of intermolecular van der Waals contacts and π–π interactions. Synergetic influence of such elastic and electrostatic interactions caused cooperative SCO in **11**.[47] The related water solvated qsal-complex—[Fe(L10)₂]·2H₂O (**12·2H₂O**)—showed a gradual and incomplete SCO with $T_{1/2}$ centred above 300 K; the de-solvated **12** showed a similar SCO behaviour to that of **12·2H₂O** except for a slight shift above 200 K as shown in Fig. 4(a).[47]

The spin-state switching behaviour of qsal-complexes—**13–17**—composed of –COOH (**L11**) or halogen (X = F (**L12**), Cl (**L13**), Br (**L14**), and I (**L15**)) substituted ligands was investigated to understand the role of intermolecular interactions and halogen substitution effects on the SCO properties. The –COOH substituted complex (**13**) showed hysteretic SCO ($T_{1/2}$ = 140 K) with a 21 K thermal hysteresis width (Fig. 4b), which is attributed to the hydrogen bond network structure originating from the COOH groups. In the halogen substituted series, complex **14** tethered with fluorine showed a temperature invariant HS state. The rest of the complexes—**15** (X = Cl), **16** (X = Br), and **17** (X = I)—underwent temperature and light-induced SCO as depicted in Fig. 4(c).[68] Complex **15** showed two-step SCO ($T^1_{1/2}$ = 308 K and $T^2_{1/2}$ = 316 K), first of its kind for (N₂O)-qsal iron(II) complexes, accompanied by symmetry breaking.[69] The complexes **16** and **17** exhibited $T_{1/2}$ = 342 K, and 295 K, respectively. Density functional theory (DFT) calculations revealed the role of π-donor halogen substituents in influencing the $T_{1/2}$ values of complexes **15–17**. However, inter-
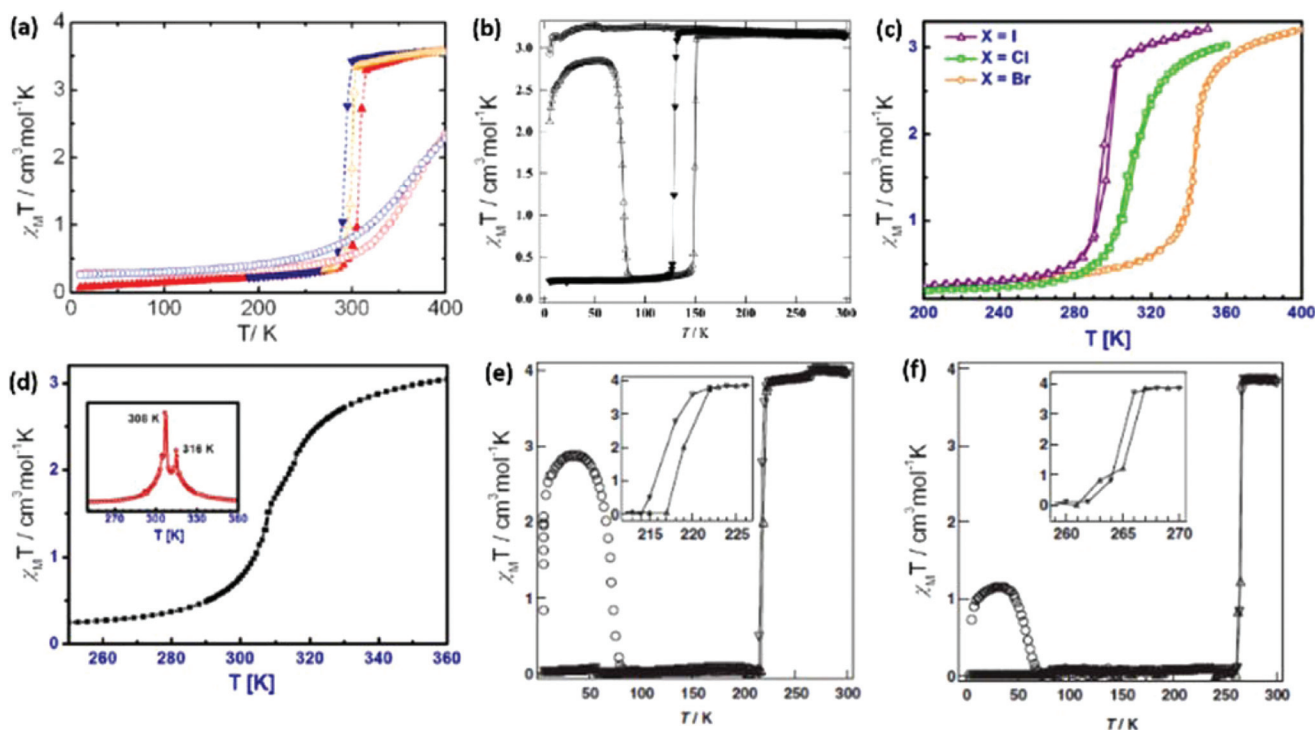
Fig. 4 $\chi_M T$ versus T plots of (a) **11**, (b) **13**, (c) **15–17**, (d) **15** showing two-step SCO behaviour, (e) **18·CH$_2$Cl$_2$** and (f) **18**. (a) Reprinted with permission from ref. 47. Copyright (2015) American Chemical Society. (c) and (d) Reprinted with permission from ref. 68. Copyright (2017) John Wiley and Sons.

molecular interactions seem to overshadow the electronic effects. In the crystal lattice of **15** and **16**, Cl and Br substituents formed C–H⋯X interactions, whereas the I⋯π interaction is observed in the I substituted complex **17**. The I⋯π interaction prevented the occurrence of a set of π–π interactions observed in the crystal lattice of **15** and **16**; these missing interactions shifted the $T_{1/2}$ of **17** to lower temperatures relative to **15** and **16**.

Cooperative and lattice solvent dependent SCO is observed in a set of qnal based complexes. The complex—[Fe(**L16**)$_2$]·CH$_2$Cl$_2$ (**18·CH$_2$Cl$_2$**)—featuring a π-extended aromatic ligand crystallized as a dichloromethane solvate. An abrupt SCO ($T_{1/2}$ = 220 K and ΔT = 2 K) was observed for **18·CH$_2$Cl$_2$**. The corresponding solvent-free complex (**18**) showed a similar abrupt SCO with $T_{1/2}$ = 265 K. The complexes are LIESST active, and a T_{LIESST} = 71 K and 57 K is reported for **18·CH$_2$Cl$_2$** and its solvent-free counterpart, respectively. A structurally related complex—[Fe(**L17**)$_2$]·(**19**)—composed of a differently oriented naphthalene group remained HS throughout the investigated temperature range demonstrating the sensitive nature of SCO to the alignment of intermolecular π–π interactions.[70]

Pyridyl-benzohydrazonate type ligands (Chart 3) are another important class of Schiff-base ligands used to prepare [Fe(N$_4$O$_2$)] type charge-neutral iron(ii)-SCO complexes. The first example of iron(ii)-pyridyl-benzohydrazonate family of complexes—[Fe(**L18**)$_2$]·CH$_3$OH (**20·CH$_3$OH**)—showed lattice solvent
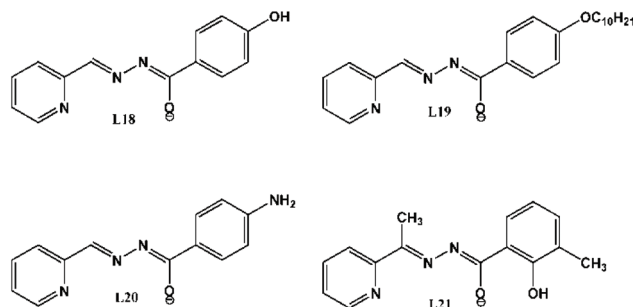
Chart 3 Structure of pyridyl-benzohydrazonate type ligands used to prepare iron(ii) complexes **20–23**.

dependent SCO. The methanol solvated complex showed abrupt and hysteretic SCO with $T_{1/2}$ = 310 K and ΔT = 60 K in the first heat-cool cycle. Subsequent cycles resulted in the loss of solvent inside the SQUID cavity, and the solvent free complex (**20**) showed $T_{1/2}$ = 282 K, ΔT = 7 K (Fig. 5(a)), and T_{LIESST} = 74 K.[71]

Alkyl chain tethered amphiphilic-SCO complexes with self-assembly propensity are of interest to prepare micro- or nano-structured SCO architectures.[72] Although SCO is observed in alkyl-tethered iron(ii) complexes,[73,74] the occurrence of hysteretic SCO in such complexes is hindered due to the, alkyl chain mediated, less-efficient propagation of structural deformations
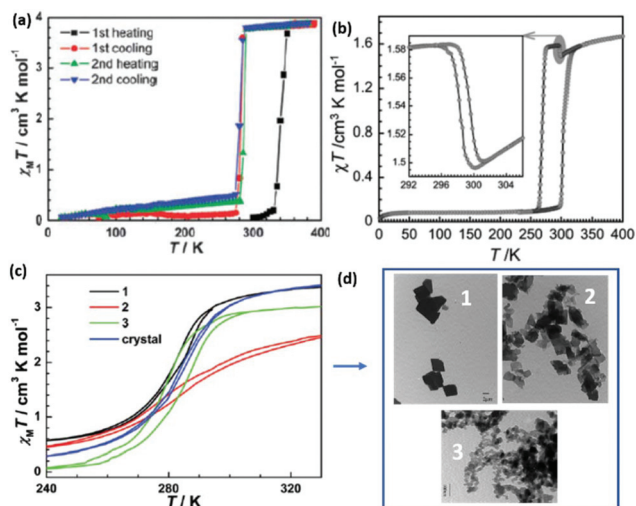
Fig. 5 $\chi_M T$ versus T plots of (a) **20·CH₃OH** and its solvent-free counterpart **20**, (b) **21**, (c) **23** in the forms of bulk crystalline solid and micro (1 and 2) – and nano (3) meter sized particles, and (d) SEM images of micro (1 and 2) and nanometer sized (3) particles of **23**. (b) Reprinted with permission from ref. 75. Copyright (2018) American Chemical Society.

Fig. 6 Structure of rhodamine 6G appended ligand **L22**, (b) intermolecular π−π interactions contributing to the occurrence of abrupt SCO in **24**, (c) $\chi_M T$ versus T plots of **24·solv** (blue trace) and **24** (red trace), and (d) luminescence-SCO correlation in **24**. Reprinted with permission from ref. 81. Copyright (2018) American Chemical Society.

of the switching core. In a rare scenario, bent-shaped iron(ɪɪ) complex—[Fe(**L19**)₂] (**21**)—tethered with C₁₀ alkyl chains showed symmetry breaking LS (monoclinic; $P2_1/n$) → HS (orthorhombic; $P2_12_12$) switching with $T_{1/2}$ = 286 K and ΔT = 35 K at a scan rate of 0.2 K min⁻¹ (Fig. 5b). The SCO is incomplete and at 400 K a 1 : 1 mixture of isolated HS and LS fractions ($\chi_M T$ = 1.67 cm³ mol⁻¹ K) is observed. A magnetic anomaly due to the conformational change of the alkyl chains accompanied SCO in the 300 K to 295 K range (Fig. 5(b)-inset). The concomitant occurrence of magnetic anomaly and hysteretic SCO rendered **21** tristable.[75]

An amino-group substituted SCO complex—[Fe(**L20**)₂] (**22**) —responsive to chemical stimuli showed a gradual SCO with $T_{1/2}$ = 320 K. Exposing the complex to HCl vapour induced the partial disassociation of the complex and consequent loss of SCO; the protonated complex remained HS throughout the measurement temperature range. Neutralization of the protonated complex by grinding it with NaOH brought back the SCO behaviour: SCO responsive to chemical stimuli was demonstrated.[76] To understand the role of size reduction on SCO parameters, complex [Fe(**L21**)₂] (**23**) was prepared as micro- and nanometer sized particles. The bulk crystalline complex showed temperature and light induced SCO with $T_{1/2}$ = 285 K and T_{LIESST} = 68 K, respectively. Unlike the bulk sample, the micro- and nanometer sized particles showed hysteretic SCO with the $T_{1/2}$ around 285 K. An increase in hysteresis width with decreasing particle size was observed owing to the increasing surface area with decreasing particle size.[77]

Functional SCO complexes appended with luminescent entities are in focus, because such systems enable the luminescence read-out of spin-states. In this context, a synergetic coupling between luminescence and spin-state is demon-

strated in molecular and polymeric SCO systems.[78–80] A recent study reported such a correlation in a family of rhodamine 6G appended complexes composed of the pyridyl-benzohydrazonate ligand **L22** (Fig. 6(a)). Complex [Fe(**L22**)₂] (ClO₄)₂·3CH₃OH·CH₂Cl₂·0.8H₂O (**24·solv**) underwent three step SCO, whereas the solvent-free complex (**24**) showed bi-stable SCO with $T_{1/2}$ = 323 K and ΔT = 40 K indicating lattice guest(s) dependent SCO as depicted in Fig. 6(c).
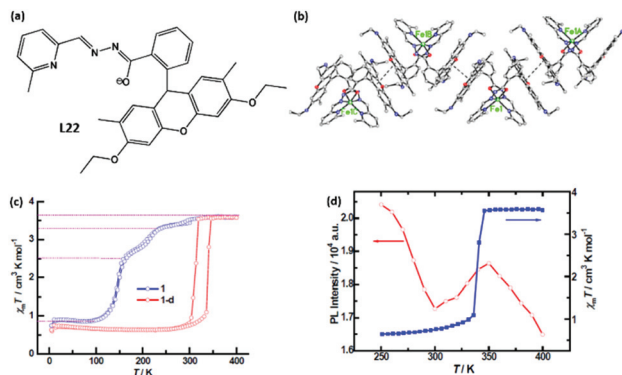
Variable temperature luminescence studies of the solvent-free complex revealed a discontinuity in the luminescence intensity (Fig. 6(d)) in the 200 K–400 K temperature range evidencing the synergetic coupling between luminescence and the spin-state.[81] A subsequent study demonstrated substituent dependent SCO and luminescence-SCO correlation in related complexes.[82]

2.3. [FeN₆]²⁺ complexes composed of bidentate imidazolylimine and tripodal tris-bidentate imidazolylamine or thiazolylimine ligands

A range of FeN₆ type mononuclear iron(ɪɪ) complexes composed of bi-, tri-, and hexadentate Schiff base ligands are reported. Imidazol-2-ylimine- and imidazol-4-ylimine-based iron(ɪɪ) complexes are a well investigated class of [FeN₆]²⁺ SCO complexes. In general, iron(ɪɪ)-imidazolyl imine complexes are prepared employing two different strategies, namely by treating bidentate imidazolylimine (Charts 4 and 5) and tripodal tris-bidentate ligands (Chart 6) with iron(ɪɪ) to form [Fe(L)₃]²⁺ and [FeL]²⁺ complexes, respectively.

In a recent review, Scott and others[45] discussed the SCO behavior of [FeN₆]²⁺ iron(ɪɪ) complexes prepared from a range of imidazolyl imine ligands and established structure–SCO property relationships. In the light of this, the discussion in this contribution is restricted to complexes showing remarkable SCO behavior such as abrupt and hysteretic SCO and stepwise spin-state switching. A discussion on chiral iron(ɪɪ)-imidazolylimine complexes is also presented to exemplify the
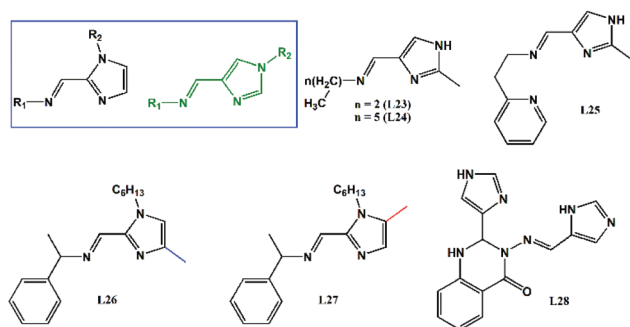
Chart 4 Structure of imidazolylimine ligands **L23–L28** used to prepare iron(ɪɪ) complexes **25–34**. The 1,3 and 1,4-imidazolylimne ligand structures are shown inside the blue box.

R₁ = n-propenyl, R2 = H: L33
R₂ = iso-butenyl, R2 = Cl: L34
R₃ = n-pentenyl, R2 = OCH3: L35
R₄ = n-hexenyl, R2 = H: L36
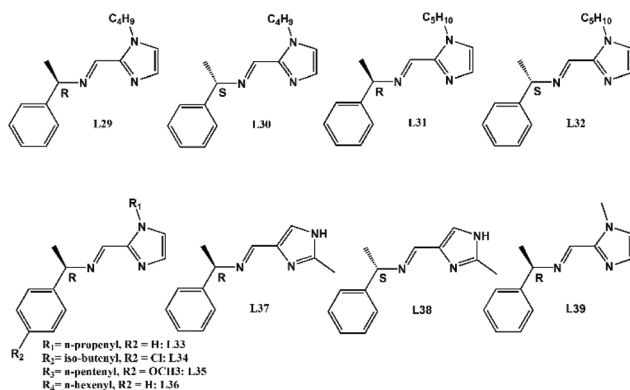
Chart 5 Structure of chiral imidazolylimine ligands **L29–L39** used in the selective preparation of Δ or Λ enantiomers of complexes **35–46**.
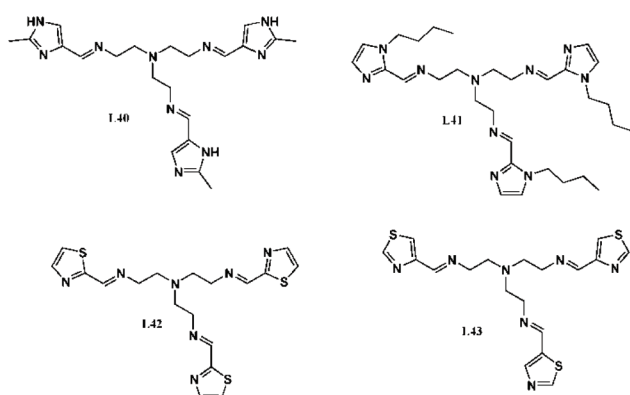
Chart 6 Structure of tripodal tris-bidentate ligands **L40–L43**.

usefulness of imidazolylimne ligands to obtain functional SCO complexes.

Anion dependent SCO behavior in a series of $[M(L)_3]^{2+}$ type iron(ɪɪ)-imidazolylimine complexes—$[Fe(L23)_3]Cl\cdot X$ (X = AsF₆ (**25**) and BF₄ (**26**)—is reported. The octahedral complexes composed of three bi-dentate **L23** ligands (Chart 4) are obtained as

facial isomers fac-$[Fe(H\ L23)_3]^{2+}$ with equal proportions of Δ and Λ enantiomers (Fig. 7a) in the crystal lattice. Hydrogen-bonding interactions between the imidazole and chloride ions (NH···Cl⁻) generated 1D ladder and 2D network assembly structures for **25** and **26**, respectively. The complex **25** featuring a larger AsF₆⁻ anion showed one-step SCO ($T_{1/2}$ = 128 K) with 4 K thermal hysteresis width as depicted in Fig. 7(c), whereas complex **26** with a relatively small BF₄⁻ anion remained in the HS state across the 300 K–5 K scan range. The AsF₆⁻ and BF₄⁻ anions, accommodated in the cavities of the hydrogen bonded network, are not involved in the formation of the network structure. However, the size of the counter anions governed the direction of the hydrogen bonds (Fig. 7(b)), which in turn affected the network propagation. Such variations in the supra-molecular organization manifested as anion dependent SCO behaviour in **25** and **26**.[83]

A similar complex—$[Fe(L23)_3]Cl\cdot PF_6$ (**27**)—was obtained as two different polymorphs. Polymorph **27-1**, prepared employing MeOH as the solvent, showed scan-rate dependent two-step hysteretic SCO. At a scan rate of 0.5 K min⁻¹, $T_{1/2}^1$ = 122 K and $T_{1/2}^2$ = 105 K were observed. The steps T^1 and T^2 are associated with ΔT = 11.3 K and 18.6 K, respectively (Fig. 7(d)). The NH···Cl⁻ hydrogen-bond mediated 1D-ladder-like self-assembled structure of polymorph **27-1** is maintained during the SCO as per the crystallographic analysis. The SCO is governed by the structural changes associated with the FeN₆ coordination sphere, anion disorder, and the conformation change of n-propyl groups.[84] Polymorph **27-2**, prepared employing EtOH as the solvent, featured a 2D-network structure and showed one-step scan rate dependent SCO as depicted in Fig. 7(e). At a scan rate of 0.5 K, $T_{1/2}$ = 143 K and ΔT = 16 K were observed.[85] A structurally related complex; fac-$[Fe(L24)_3]Cl\cdot PF_6$ (**28**) showed three-step SCO. At a scan rate of 0.5 K, $T_{1/2}^1$ = 124 K (ΔT = 14.4 K), $T_{1/2}^1$ = 141 K (ΔT = 6.3 K), and $T_{1/2}^1$ = 153 K (ΔT = 2.4 K) were obtained. In the crystal lattice, the complex entities self-organized as a tetrameric cubane-like structure—$[fac$-$\{Fe(L_{24})_3\}^{2+}\cdots Cl]_4$—constructed from twelve NH···Cl hydrogen bonds. The three-step SCO observed in the complex is tentatively attributed to the stepwise switching of the iron(ɪɪ) centers residing in the cubane-like structures.[86]

Anion-dependent SCO is demonstrated in another series of complexes—$[Fe(L25)_3]Cl\cdot X$ (X = PF₆ (**29**), ClO₄ (**30**), and BF₄ (**31**). Steeper SCO profiles were obtained with decreasing anion size—PF₆⁻ > ClO₄⁻ > BF₄⁻. However, a linear anion size dependence of $T_{1/2}$ is not observed for the complexes: **29** ($T_{1/2}$ = 154 K, ΔT = 3.5 K), **30** ($T_{1/2}$ = 185 K, ΔT = 1.5 K), and **31** ($T_{1/2}$ = 147 K, ΔT = 1.8 K).[87]

Structural isomers—fac-Λ-$[Fe(L26)_3](ClO_4)_2$ (**32**) and fac-Λ-$[Fe(L27)_3](ClO_4)_2$ (**33**)—featuring methyl groups at the 4- and 5-positions, respectively, of the imidazole ring were prepared employing ligands **L26** and **L27**. The complexes crystallized as solvent-free fac-Λ-enantiomers, and a similar crystal packing is observed. Complex **33** showed partial SCO ($T_{1/2}$ = 390 K), whereas **32** remained HS and no SCO is observed. A sterically crowded coordination environment around iron(ɪɪ) due to the close proximity of the methyl group to the coordinating imid-
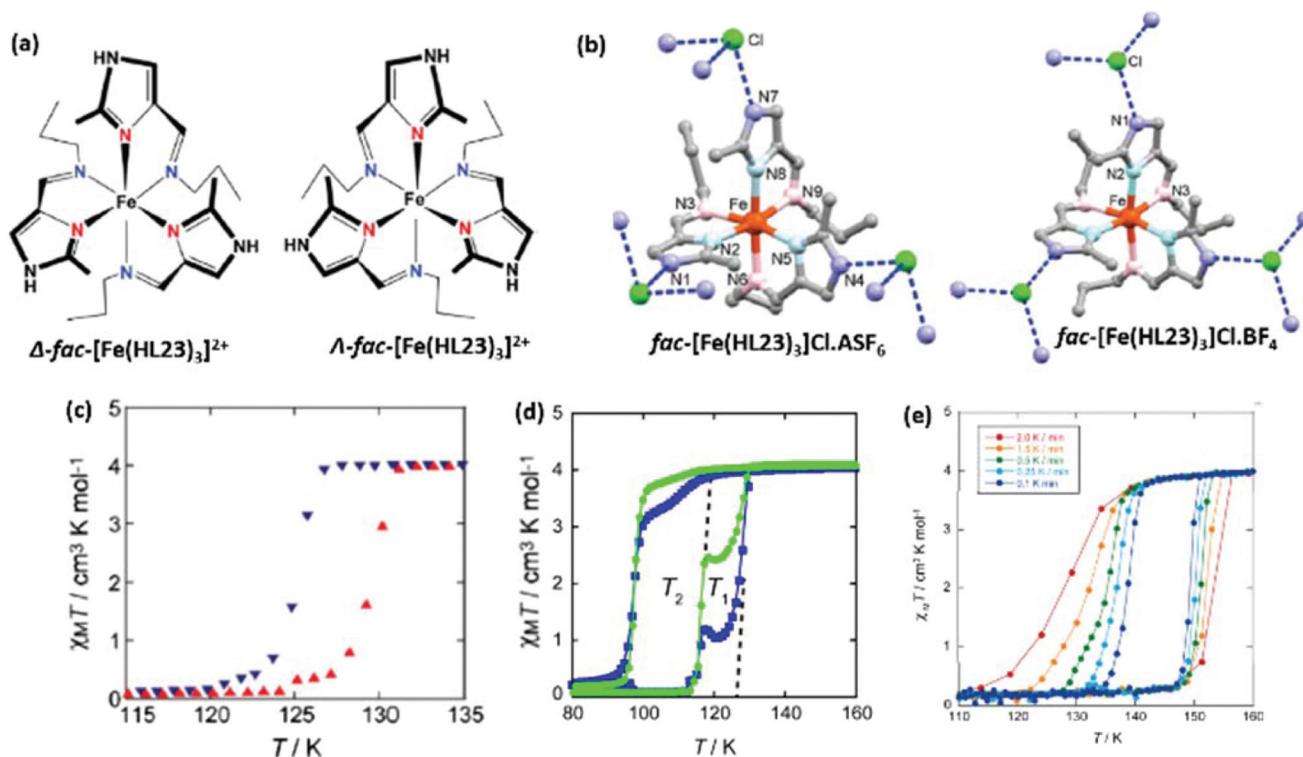
Fig. 7 (a) Δ and Λ isomers of 25, (b) hydrogen bonding modes in 25 and 26, and $\chi_M T$ versus T plots of (c) 25 and (d) 27-1, and (e) scan rate dependent SCO of 27-2. (d) Reprinted with permission from ref. 84. Copyright (2015) American Chemical Society. (a) and (e) Reprinted with permission from ref. 85. Copyright (2017) Elsevier.

azole nitrogen trapped 32 in the HS state. On the other hand, the placement of the methyl group at the 5-position of the imidazole ring in 33 produced a relatively less crowded coordination environment around iron(II) thereby stabilizing the LS state. Thus, the role of steric crowding in influencing the spin-state in isomeric coordination complexes was demonstrated.[88]

The synthesis, structural investigation, and SCO behavior of [Fe(L)$_2$]$^{2+}$ iron(II) complexes—[Fe(L28)$_2$](BF$_4$)$_2$·(Et$_2$O)(34·Et$_2$O) and [Fe(L28)$_2$](BF$_4$)$_2$·3H$_2$O (34·3H$_2$O)—derived from a tridentate imidazolylimine-based ligand L28 were reported by Huang and others. Each mer-L28 coordinates to the iron(II) equatorially through imidazole nitrogen donors and axially by the imine nitrogen donors. The Fe–N bond-length in 34·Et$_2$O is smaller than the Fe–N bond-length of 2.15 Å observed for a HS iron(II) complex. But this value is larger than that expected for LS iron(II), indicating the co-existence of LS- and HS-states. Complex 34·Et$_2$O showed a gradual and incomplete SCO with $\chi_M T$ = 2.28 cm^3 kmol^{-1} at 350 K for the first cycle; $T_{1/2}$ = 305 K was observed. The second heating and cooling cycles produced a small hysteresis loop, which is attributed to a partial removal of the Et$_2$O solvent. Complex 34·3H$_2$O showed gradual, hysteretic, and complete above-RT SCO with $T_{1/2}$ = 346 K and ΔT = 20 K. The complexes were also LIESST active at 5 K and showed T_{LIESST} = 70 K (34·Et$_2$O) and 40 K (34·3H$_2$O). However, only 8% and 10% LS → HS transition efficiency is observed for 34·Et$_2$O and 34·3H$_2$O, respectively due to the short life-time of the light-induced excited HS states.[89]

Recently, multifunctional SCO complexes have attracted much interest due to their utility to obtain SCO-based device architectures. Chirality is an important molecular property, and by combining the SCO property with chirality, novel hybrid materials displaying magneto-chiral dichroism and ferroelectricity could be realized.[8] Furthermore, chirality dependent SCO behaviour in molecular complexes could be obtained considering the sensitive nature of SCO to intermolecular interactions. Thus, its desirable to have chiral SCO complexes both in terms of applications and from a fundamental scientific point of view.

The fac-bidentate helical coordination mode of imidazolylimine ligands produces Δ and Λ isomers of [FeN$_6$]$^{2+}$ complexes as discussed above. However, equal proportions of Δ and Λ isomers were observed in the crystal lattice of most of the complexes discussed above. Notable exceptions are complexes 32 and 33, whose crystal lattice is composed exclusively of Λ-enantiomers. The use of chiral imidazolylimine ligands induced selective crystallization of either Δ or Λ enantiomers of fac-[FeN$_6$]$^{2+}$ complexes as detailed below.

The spin-state switching behaviour of enantiomers, co-enantiomers, racemates, and co-racemates of chiral imidazolylimine-based iron(II) complexes is reported. First, two sets of enantiomeric complexes—(i) fac-Λ-[Fe(R-L29)$_3$](ClO$_4$)$_2$ (35) and fac-Δ-[Fe(S-L30)$_3$](ClO$_4$)$_2$ (36) (Fig. 8a); (ii) fac-Λ-[Fe(R-L31)$_3$](ClO$_4$)$_2$ (37) and fac-Δ-[Fe(S-L32)$_3$](ClO$_4$)$_2$ (38) (Fig. 8b)—were prepared by performing a multi-component self-assembly reac-
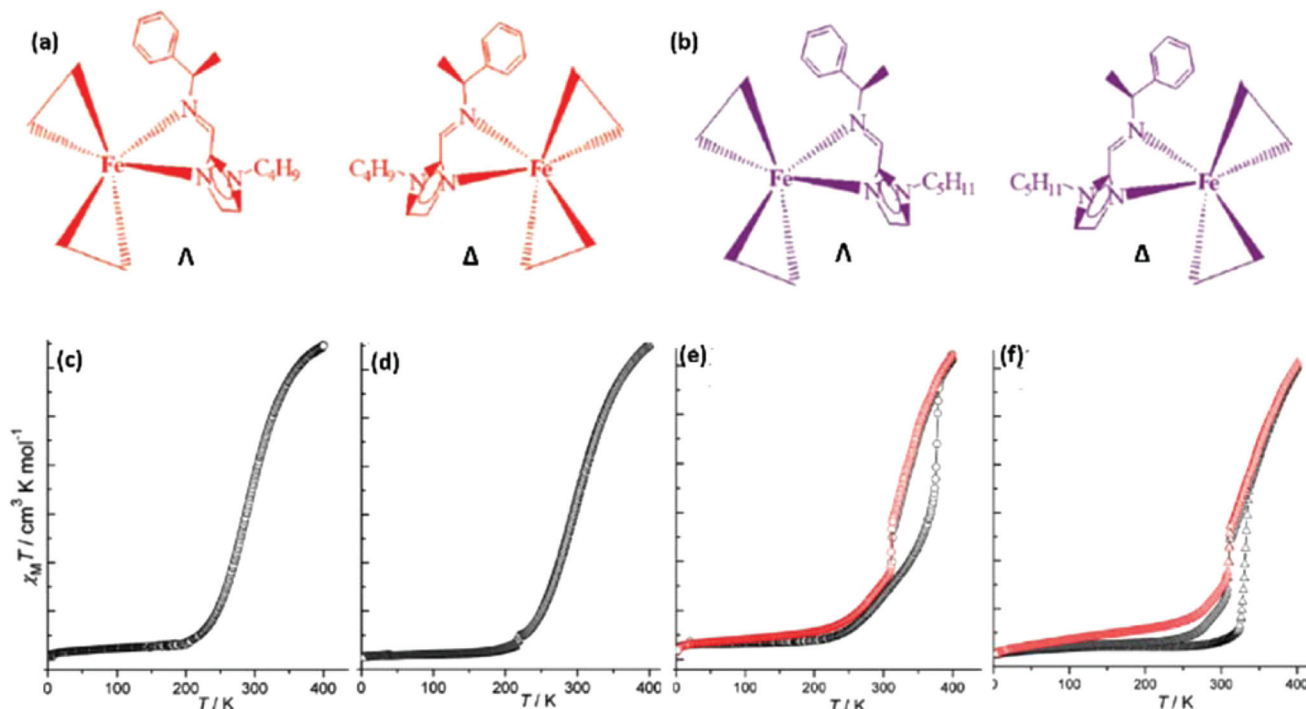
Fig. 8 (a) and (b) Structure of *fac-Λ and fac-Δ* isomers **35–38**, $\chi_M T$ *versus T* plot of (c) **37R**, (d) **35R37R**, (e) **37R38S**, and (f) **35R36S37R38S**.

tion by treating together chiral phenylethylamine (R or S), 1-alkyl-2-imidazolecarboxaldehyde, and Fe(ClO$_4$)$_2$·6H$_2$O. Subsequent co-crystallization of the enantiomers resulted in the formation of co-enantiomers: **35R37R** ($ΛΛ$) and **36S38S** ($ΔΔ$); racemates: **35R36S** ($ΛΔ$) and **37R38S** ($ΛΔ$); and co-race-mate: **35R36S37R38S** ($ΛΔΛΔ$).

Enantiomers **35** and **36** remained HS throughout the measurement temperature range of 2 K–400 K. A gradual and complete SCO ($T_{1/2}$ = 291 K) is observed for enantiomers **37** and **38**, respectively. The co-enantiomeric complex **35R37R** also showed a gradual, reversible, and complete SCO around room temperature but with $T_{1/2}$ shifted upward to 301 K. The racemate **35R36S** showed a gradual and incomplete SCO with $T_{1/2}$ = 336 K, and the racemate **37R38S** exhibited a 46 K wide hyster-esis loop as depicted in Fig. 8(e). The co-racemate **35R36S37R38S** showed an incomplete and above RT SCO ($T_{1/2}$ = 330 K) with a hysteresis loop of 11 K (Fig. 8(f)).[90] In an interesting scenario, the chiral iron(II) complex—*fac-Δ*-[Fe(S-**L30**)$_3$](BF$_4$)$_2$ (**39**)—was obtained as two solvent free polymorphs. In the dark purple poly-morph **39-I**, the edge-to-face C–H⋯π interactions between the phenyl C–H and the neighbouring phenyl ring involve the H-atom located at the *meta* position of the phenyl ring. Such edge-to-face C–H⋯π interactions in polymorph **39-II** involve the H-atom located at the *para*-position of the phenyl ring. Ploymorph **39-I** underwent gradual SCO with $T_{1/2}$ = 294 K, and **39-II** was trapped in the HS state in the 400 K–5 K temperature range. Remarkably, the HS polymorph **39-II** showed ferroelectric behaviour due to the polar (C_3) point group associated with it.[91]

Four homochiral-iron(II) SCO complexes, **40–43** were obtained from *in situ* generated chiral ligands—(R)-**L**n (n =

33–36). The complexes **40**, **42**, and **43** were obtained as *fac-Λ* isomers, whereas **41** was obtained as a *fac-Δ* isomer. Complexes **40** and **43** showed a reversible, gradual and, com-plete SCO with $T_{1/2}$ = 257 K and 282 K, respectively. An incom-plete and gradual SCO is observed for **41** and **42** with $T_{1/2}$ = 375 K and 137 K, respectively. However, **41** showed steeper SCO than **42**. Complexes **41** and **43** with a lower symmetry exhibited one-step SCO at a relatively higher temperature range than that of **40** and **42**. The different SCO behaviour of com-plexes **40–43** was attributed to the substitution effect, packing mode, and intermolecular interactions. The electronic substi-tution effect arises due to the varying nature of functional groups (R^2 = –H (**40**), –Cl (**41**), and –OCH$_3$ (**42**)) placed on the amine moiety, which modified the ligand-field strength around the iron(II) affecting the nature of SCO. Apart from the electronic effect, packing modes certainly exerted an obvious influence on the SCO behaviour. Significant differences in the crystal packing of complexes **40–43** were observed due to the differing substitution pattern of the complexes. Various inter-molecular C–H⋯π interactions between the imidazole and phenyl rings in **40** and **43** are observed. Remarkably, **41** exhibi-ted a relatively stronger C–Cl⋯π intermolecular interaction, which raised the $T_{1/2}$ value of **42** relative to other complexes. In the series **40–43**, the strength of the intermolecular interaction seems to be a dominating factor in deciding the $T_{1/2}$ value.[92]

The ligand chirality mediated selective preparation of *fac-Λ* and *fac-Δ* enantiomers was reported. Ligands R-**L37** and S-**L38** favoured the selective formation of *fac-Λ*-**44** and *fac-Δ*-**45** enan-tiomers, respectively. The crystalline *fac-Λ*-**44** with a co-crystal-lized EtOH showed complete and cooperative SCO with $T_{1/2}$ =

195 K; the SCO behaviour of *fac-Δ-45* is not reported. Thus, it is not possible to discern the enantiomer dependence of SCO.[93]

The chiral resolution of racemic lactonitrile (LN) and methylglutaronitrile (MGN) by a homochiral SCO complex—*fac-Λ*-[Fe(*R*-**L39**)₃](ClO₄)₂·MeCN (**46**)—was demonstrated. The complex cations are stacked into a left-handed double helix supramolecular structure with MeCN solvent guests filling the helical channel. Complex **46** showed gradual SCO with $T_{1/2}$ = 355 K in the first heating mode. In the subsequent cycles, $T_{1/2}$ = 217 K is observed due to the loss of lattice MeCN. Dissolution of **46**·MeCN in racemic LN or MGN led to the formation of triple helical **46**·1/3(*R*)-LN and **46**·1/3(*S*)-MGN crystals with *R*-LN and *S*-MGN located in the helical channel. The **46**·1/3(*R*)-LN and **46**·1/3(*S*)-MGN showed incomplete SCO behaviour with $T_{1/2}$ = 363 K, and no solvent loss is observed The space group difference between **46**·MeCN ($P2_1$) and **46**·1/3(*R*)-LN/**46**·1/3(*S*)-MGN ($P2_12_12_1$) complexes is attributed as the reason behind the different spin-state switching behaviour of the complexes.[94]

2.4. [FeN₆]²⁺ complexes composed of tripodal tris-bidentate imidazolylamine and thiazolylamine ligands

Iron(II) complexes based on tripodal tris-bidentate-imidazolylimine and -thiazolylimine ligands (Chart 6) showing remarkable SCO behaviour were reported. A correlation between the SCO behaviour and relative size of the anions is established in a series of complexes: [Fe(**L40**)]Cl·X (X⁻ = PF₆ (**47**), AsF₆ (**48**), SbF₆ (**49**), and CF₃SO₃ (**50**)). In each complex, the NH···Cl hydrogen bonding interactions between the chloride ion and NH groups of imidazole corresponding to three neighbouring complex cations resulted in the formation of a 2D-extended network structure. The anion occupied the space between the 2D-sheets, whose structure is affected by the size and shape of the anion, causing modifications of the spin-state switching behaviour. One-step incomplete and two-step complete SCO behaviour were observed for **47** ($T_{1/2}^1$ = 122 K) and **48** ($T_{1/2}^2$ = 82 K), respectively. On the other hand, complexes **49** ($T_{1/2}$ = 117 K) and **50** ($T_{1/2}$ = 82 K) showed a gradual and steep one-step SCO behaviour, respectively. A small 4 K thermal hysteresis loop was observed for **50** at a scan rate of 1 K min⁻¹. The $T_{1/2}$ values of the complexes decreased with increasing anion size, that is, from PF₆⁻ to CF₃SO₃⁻.

In an interesting study, two separate cooperative SCO behaviours mediated by kinetically controlled phase transition involving the conformational change of the *n*-butyl chains and the associated reorganization of the intermolecular interactions were demonstrated. The complex, [Fe(**L41**)](PF₆)₂ (**51**) showed abrupt and hysteretic SCO with $T_{1/2}$ = 122 K and ΔT = 14 K at a scan rate of 4 K min⁻¹. On the other hand, $T_{1/2}$ = 156 K and ΔT = 41 K were observed at a scan rate of 0.1 K min⁻¹.

The occurrence of a temperature lag due to the freezing-in of the HS state during the HS to LS (LS1) switching caused the lower $T_{1/2}$ value observed for the faster scan. At a scan rate of 0.1 K min⁻¹, spin-state switching involves an additional LS state (LS2), and SCO at 0.1 K min⁻¹ scan rate is best described as the one involving the same HS state and two different LS states, namely LS1 and LS2 as depicted in Fig. 9(c). Crystal struc-
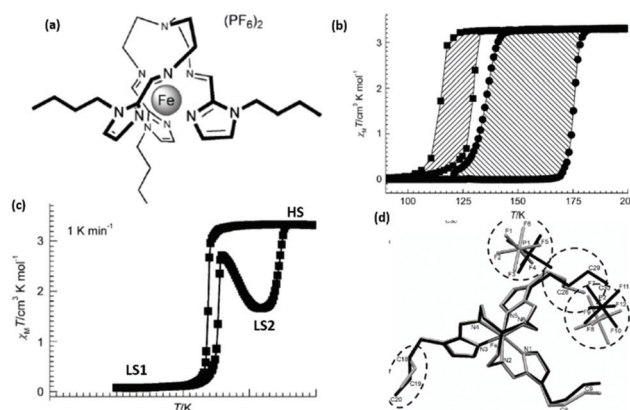
Fig. 9 (a) Structure of **51**, (b) $\chi_M T$ versus T plots of **51** at 4 K min⁻¹ (filled squares) and 0.1 K min⁻¹ (filled circles), (c) $\chi_M T$ versus T plot of **51** at 1 K min⁻¹ showing the intermediate LS phase—LS2, and (d) superimposed structure of **51** at LS1 and LS2 phases showing alkyl chain conformation variation. Reprinted with permission from ref. 61. Copyright (2013) John Wiley and Sons.

ture analysis of **51** at LS1 (110 K) and LS2 (130 K) states revealed marked differences in the conformations of the alkyl chains (Fig. 9(d)) as well as the relative positions of the counter-anions. These remarkable variations in the conformation of alkyl chains induced different intermolecular interactions, which facilitated the access of the LS2 state at the lower scan rate thereby a larger hysteresis width is obtained at 0.1 K min⁻¹.[61]

SCO in [FeL]²⁺ type complexes featuring tripodal tris-bidentate thiazolylimine ligands was also studied. The commonly observed NH···Cl hydrogen-bonding interactions in the above-discussed imidazolylimine-based complexes are absent in thiazolylimine complexes due to the absence of the N–H hydrogen bond donor in the thiazolylimine ligand. However, SCO is no less spectacular in thiazolylimne-based complexes. Anion dependent SCO in a series of solvent-free [Fe(**L42**)](X)₂ (X⁻ = BF₄ (**52**), SbF₆ (**53**), and CF₃SO₃ (**54**)) complexes was reported. Complexes **53** (SbF₆) and **54** (CF₃SO₃) having relatively larger anions showed gradual and incomplete SCO, respectively. On the other hand, an abrupt and hysteretic SCO was observed for complex **52** with a relatively smaller charge balancing BF4⁻ anion; $T_{1/2}$ = 270 K and ΔT = 3 K were obtained at a scan rate of 1 K min⁻¹. More intermolecular interactions between [Fe(**L42**)]²⁺ entities in **52**, relative to the complex cations of **53** and **54**, inferred from the crystallographic analysis of the complexes, explains the abrupt SCO of **52**. Low-spin six-coordinate complexes **53** and **54** crystallized as enantiomerically pure Λ and Δ enantiomers, respectively from an acetonitrile-ether solvent system; a chiral space group $Pbc2_1$ (**53**) and $P6_5$ (**54**) was observed. However, the six-coordinate LS-**52** crystallized in the achiral space group—$P2_1/C$ from the acetonitrile-*tert*-butyl-methyl ether solvent system. Remarkably, the HS-**52** crystallized as a seven-coordinate complex involving a new Fe–N (bridgehead) bond: a change in the coordination number—from six to seven—upon LS → HS switching was revealed.[95] A similar complex [Fe(**L43**)](BF₄)₂ (**55**) crystallized as a racemate

from the ethanol–ether solvent mixture. Complex **55** showed a re-entrant symmetry-breaking gradual SCO with $T_{1/2}$ = 208 K.[96]

2.5. [FeN₆] complexes composed of triazole-based bidentate and tripodal tris-bidentate ligands

Schiff base ligands composed of the 1,2,3-triazole ring offer suitable ligand field strength to obtain SCO active iron(ɪɪ) complexes. Some examples of iron(ɪɪ) SCO complexes composed of
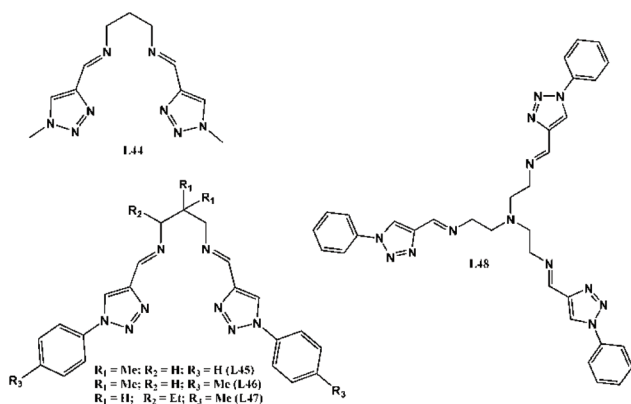
Chart 7 Structures of 1,2,3-triazole based ligands employed to prepare iron(ɪɪ) complexes **56–60**.

1,2,3-triazole-based tetradentate and tripodal tris-bidentate ligands are discussed as follows (Chart 7).

Polymorphism-dependent hysteretic SCO is demonstrated in [Fe**L44**(NCS)₂] (**56**). The tetradentate **L44** coordinates the iron(ɪɪ) at equatorial positions, and anionic NCS⁻ ligands coordinate *via* nitrogen donors and occupy the axial positions to produce a charge-neutral complex. Remarkably, two solvent-free polymorphs of **56**—**56-I** and **56-II**—were obtained. Treating methanol solutions of **L44** and Fe(NCS)₂ together simultaneously yielded **56-I** and **56-II**. Exclusive crystallization of **56-II** was achieved by treating a CHCl₃ solution of **L44** with a MeOH solution of Fe(NCS)₂. The orange polymorph **56-I** is HS at RT and showed abrupt and hysteretic SCO with $T_{1/2}$ = 270 K and ΔT = 2 K. The dark purple-red polymorph **56-II** is LS at RT and showed similar abrupt and hysteretic SCO (ΔT = 2 K) as **56-I**. However, a 101 K upward shift of the switching temperature ($T_{1/2}$ = 371 K) is observed for **56-II** relative to **56-I** (Fig. 10(a)). Crystallographic analysis of the polmorphs **56-I** and **56-II** revealed significant differences in the packing modes. In **56-I**, C–H⋯S hydrogen-bonding interactions produced an extended 3D-network structure (Fig. 10(b)). On the other hand, the 3D-network of **56-II** is constituted of C–H⋯S and C–H⋯N hydrogen-bonding interactions. The existence of the additional C–H⋯N and differently organized C–H⋯S hydrogen-bonding interactions in **56-II** relative to **56-I** caused the observed 100 K increase in $T_{1/2}$ of **56-II**.[97]
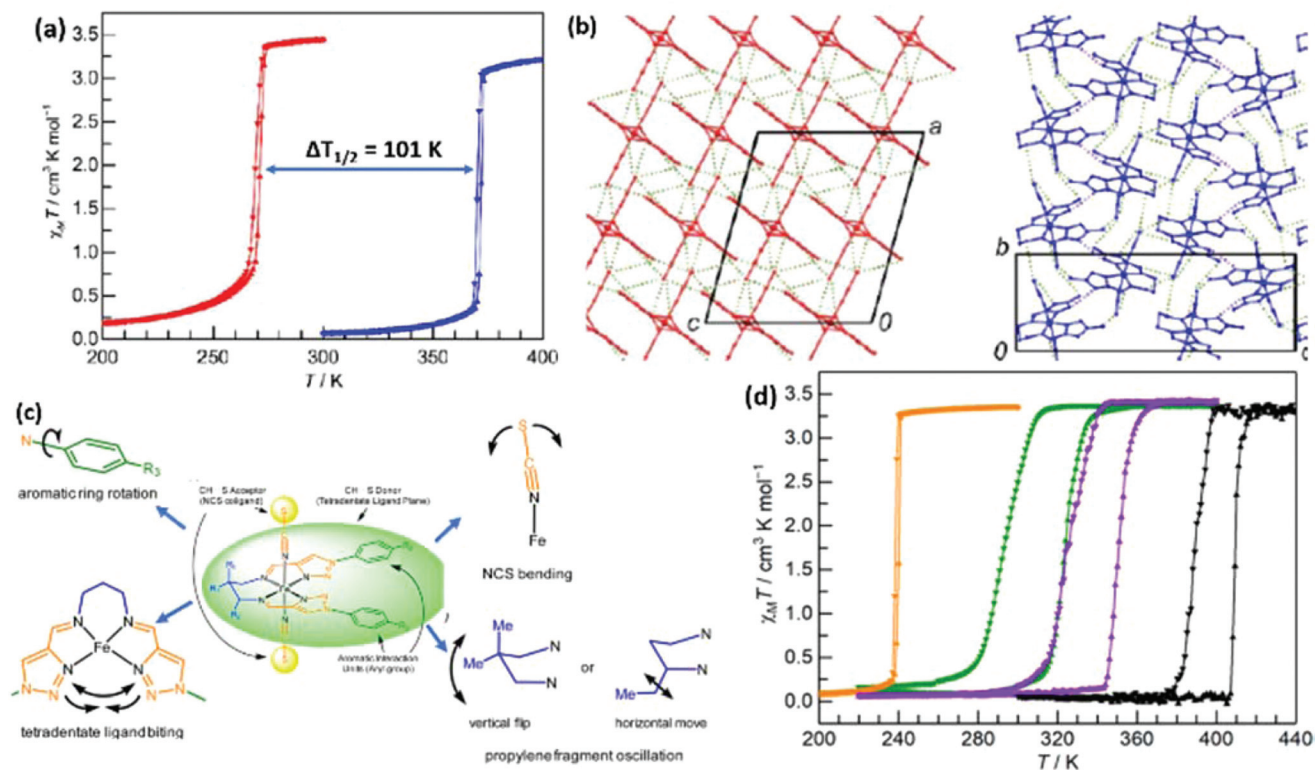
Fig. 10 (a) $\chi_M T$ *versus* T plots of **56-I** (red) and **56-II** (blue), (b) packing arrangement in the crystal lattice of **56-I** (left) and **56-II** (right), (c) structural features contributing to the crystal engineering approach used to design bi-stable SCO complexes: **57–59**, and (d) $\chi_M T$ *versus* T plots of complexes **57** (black), **58** (orange), **59a** (purple), and **59b** (green). Reprinted with permission from ref. 37. Copyright (2017) American Chemical Society.

A crystal engineering approach based on concerted molecular motions of the ligand backbone (Fig. 10(c)) was employed to prepare 1,2,3-triazole-based bi-stable iron(II) SCO complexes: [FeL$_{45}$(NCS)$_2$] (**57**), [FeL$_{46}$(NCS)$_2$] (**58**), [FeL$_{47}$(NCS)$_2$]·0.5H$_2$O (**59a**), and [FeL$_{47}$(NCS)$_2$]·0.5CH$_3$CN·0.5CH$_3$OH·H$_2$O (**59b**). All the complexes showed stable bi-stable SCO behavior upon repeated cycling. The solvent free complexes **57** ($T_{1/2}$ = 399 K and ΔT = 20 K) and **58** ($T_{1/2}$ = 240 K and ΔT = 1 K) showed abrupt and hysteretic SCO at above and below RT, respectively (Fig. 10(d)). The solvated complexes **59a** and **59b** showed SCO at RT and above RT, respectively, with $T_{1/2}$ = 338 K (**59a**) and 309 K (**59b**); ΔT = 26 K (**59a**) and 31 K (**59b**) as shown in Fig. 10(d). In all the complexes, weak C–H···S hydrogen-bonding interactions facilitated the formation of 3D-network structures incorporating additional C–H···π and π···π interactions. Such intermolecular interactions and flexible nature of ligand backbones **L45–L47** promoted bi-stable SCO behaviour in complexes **57–59**.[37] Complex [FeL$_{48}$] (NTf)$_2$ (**60**) composed of tripodal tris-bidentate ligand **L48** showed a gradual SCO with $T_{1/2}$ = 280 K.[98]

2.6. Other remarkable examples

Reversible spin-state dependent rupture and formation of an Fe–N bond was demonstrated in some families of iron(II) complexes composed of macrocyclic Schiff base ligands. Such a process increases the lifetime of the LIESST generated HS state and renders the complexes suitable for applications. Complex [FeL$_{49}$(CN)$_2$]·MeOH (**61·MeOH**) derived from the macrocyclic Schiff base ligand **L49** (Fig. 11(a)) and axially coordinating CN$^-$ *via* carbon donors is LS in the 300 K to 5 K temperature range. Upon excitation with white or green light at low temperatures, LIESST mediated population of the metastable HS state showing a HS → LS relaxation rate of 0.3 K min^{-1} was observed. The observed T_{LIESST} = 140 K is remarkably higher than the usual 50 K–80 K range observed for iron(II) SCO complexes. An explanation based on coordination number change in concert with HS → LS switching/relaxation was proposed to account for the high T_{LIESST} observed in **61·MeOH**. A recent

crystallographic study confirmed the above attribution by characterising the HS **61·MeOH** as a seven-coordinate complex as depicted in Fig. 11(b). In essence, the coordination number change, from seven (HS) to six (LS), associated with thermal relaxation of the LIESST produced HS state to the thermodynamic LS state increased the lifetime of the metastable HS state of **61·MeOH**.[99]

A recently reported charge neutral complex—[Fe(**L50**)$_2$ (NCSe)$_2$](**62**)—showed stable and hysteretic SCO behaviour with $T_{1/2}$ = 286 K and ΔT = 41 K at a scan rate of 2 K min^{-1} (Fig. 11(d)). Crystallographic studies of the complex at 300 K (HS) and 230 K (LS) revealed a structural transition from monoclinic $P2_1/c$ (HS) to $Pccn$ (LS).[100] The analogous complex [Fe(**L50**)$_2$(NCS)$_2$] (**63**) showed SCO with $T_{1/2}$ = 211 K and ΔT = 41 K. Complex **62** is not LIESST active, whereas a small effect was observed for **63**.

3. An outlook on the SCO behaviour of multinuclear and 1D-polymeric SCO complexes based on Schiff base ligands

Apart from the above discussed mononuclear complexes, SCO in multinucler iron(II) complexes composed of Schiff base ligands is also studied. Supramolecular interactions such as hydrogen bonding and π–π interactions contribute to abrupt and hysteretic SCO in mononuclear complexes. On the other hand, the nature of spin-state switching in multinuclear iron(II) complexes is governed by intramolecular interactions mediated by ligand back bones connecting switching iron(II) centres and intermolecular contacts between discrete switching entities.

3.1. Multinuclear complexes

Among multinuclear iron(II) complexes, dinuclear systems are a well-studied class, especially to obtain stepped [LS–LS] → [LS–HS] → [HS–HS] spin-state switching. Some examples belonging to two major classes of binuclear SCO systems—triply- and doubly stranded iron(II) helicates—showing abrupt and hysteretic SCO are discussed as follows.

Ligand **L51** (Chart 8) was used to prepare dinuclear triple helicate iron(II) complexes—[Fe$_2$(**L51**)$_3$](ClO$_4$)$_4$·5CH$_3$NO$_2$ (**64**) and [Fe$_2$(**L51**)$_3$](BF$_4$)$_4$·6.5CH$_3$NO$_2$·0.5H$_2$O (**65**). Complex **64** crys-
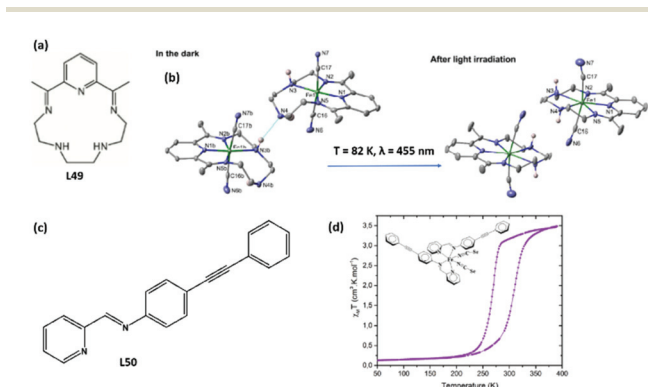
Fig. 11 (a) Structure of **L49**, (b) X-ray structures of LS and HS states of **61·MeOH** showing coordination number change upon LIESST mediated LS → HS switching, (c) structure of **L50**, and (d) $\chi_M T$ versus T plot of **62**; the inset shows the structure of **62**. Reprinted with permission from ref. 58. Copyright (2018) American Chemical Society.
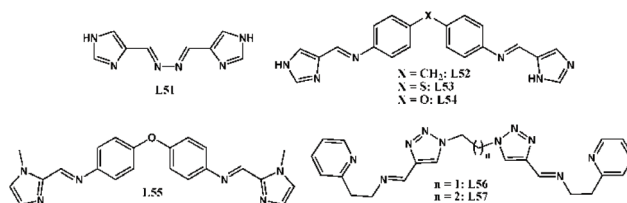
Chart 8 Structures of imidazolylimine (**L51–L55**) and 1,2,3-triazole (**L56** and **L57**) ligands used to prepare dinuclear iron(II) complexes.

tallized in the centrosymmetric space group $P2_1/C$ and the crystal lattice was composed of equal proportions of homochiral Λ–Λ and Δ–Δ pairs indicating the absence of spontaneous chiral resolution. A zigzag 1D-self-organization along the crystallographic c-axis was observed due to the hydrogen bonding interactions between the neighbouring dinuclear units, which also placed the iron(II) centres in the helicate at a slightly different crystallographic environment. The triple helicate complex (**65**) featuring BF_4^- anions crystallized as needle and block polymorphs, and the crystal structure of the block polymorph, crystallized in the centrosymmetric space group $P\bar{1}$, was reported. As in the case of **64**, a heterochiral/racemic lattice was observed for **65**. However, hydrogen bonding interactions in the crystal lattice of **65** produced a 2D-sheet like self-organization along the crystallographic c-axis. Complexes **64** and **65** showed incomplete/half SCO behaviour, that is, the expected complete [LS–LS] → [LS–HS] → [HS–HS] switching is not observed. Instead, a stable mixed [LS–HS] phase associated with a distinct dinuclear helicate was reported below 220 K and 180 K for **64** ($\chi_M T$ = 3.3 cm^3 K mol^{-1}) and **65** ($\chi_M T$ = 3.7 cm^3 K mol^{-1}), respectively. Complex **64** underwent the [LS–HS] → [HS–HS] switching with $T_{1/2}$ = 240 K. Remarkably, complex **65** showed the [LS–HS] → [HS–HS] switching ($T_{1/2}$ = 187 K) with a 7 K thermal hysteresis loop at a scan rate of 2 K min^{-1}. The 2D-sheet like self-organization involving stronger hydrogen bonding interactions in **65** compared to the 1D-organization observed in **64** is a contributing factor promoting abrupt and hysteretic SCO in **65**.[101]

Craze and others reported a series of binuclear iron(II)-Schiff base SCO complexes—[Fe$_2$(**L52**)$_3$](BF$_4$)$_2$ (**66**), [Fe$_2$(**L53**)$_3$] (BF$_4$)$_2$ (**67**), and [Fe$_2$(**L54**)$_3$](BF$_4$)$_2$ (**68**)—based on ligands **L52**–**L54** (Chart 8). The effects of the steric properties of three different central ligand atoms (–X–, X = –CH$_2$–, –S–, or –O–) on the structure and SCO of their respective helicate architectures were investigated. All the three helicates displayed a gradual and incomplete SCO from the mixed [LS–HS] state to [HS–HS] state. The heating and cooling modes resulted in a small hysteresis for all the three helicates as shown in Fig. 12(b). For **66**, the $\chi_M T$ versus T plot in the cooling mode is in accordance with the occurrence of half [HS–HS] → [LS–HS] SCO with a broad transition happening between 60 K to 250 K. The $\chi_M T$ value of 7.71 cm^3 K mol^{-1} observed at RT corresponds to two magnetically uncoupled octahedral iron(II) centres in the helicate. As the temperature is lowered, $\chi_M T$ remained constant until 250 K and then dropped in a single step with a $T_{1/2\downarrow}$ of 155 K ($\chi_M T$ = 4.41 cm^3 K mol^{-1} at 50 K). This indicates incomplete SCO with around 40% of the iron(II) centres in the LS state. In the heating mode $T_{1/2\uparrow}$ = 170 K is observed resulting in a thermal hysteresis of 15 K. The compound **68** also showed gradual SCO with $T_{1/2}$ = 150 K and 165 K for the cooling and heating cycles, respectively, with a 15 K hysteresis loop. The RT $\chi_M T$ value of 7.67 cm^3 K mol^{-1} is in accordance with the complete HS–HS state of the iron(II) centres; the $\chi_M T$ = 3.92 cm^3 K mol^{-1} at 50 K indicates approximately half-completed SCO. Complex **67** (X = S) showed abrupt SCO from the mixed [LS–HS] state (Fig. 12(a)) to [HS–HS] state. The complex is HS at RT
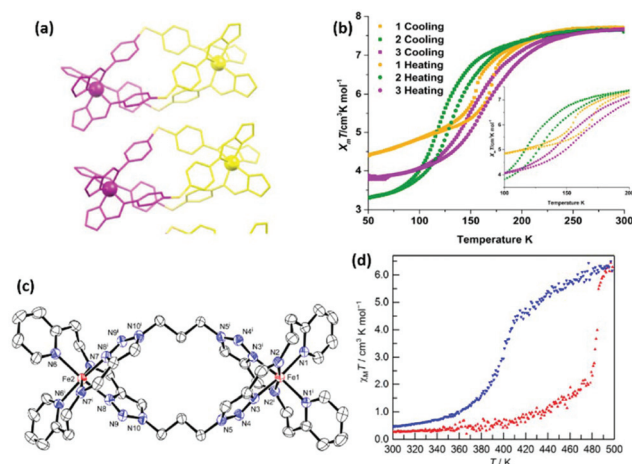
Fig. 12 (a) Packing picture of dinuclear triple helicate complex **67** at 100 K showing distribution of HS (yellow) and LS (purple) iron(II) centres, (b) $\chi_M T$ versus T plot of **66** (yellow), **67** (green), and **68** (purple), (c) ORTEP diagram of dinuclear double helicate **71**, and (d) $\chi_M T$ versus T plot of **71**.

($\chi_M T$ = 7.65 cm^3 K mol^{-1}) and showed an abrupt one-step SCO behaviour with $T_{1/2}$ = 123 K and ΔT = 15 K.[102]

Remarkably, a complete [LS–LS] → [HS–HS] switching is observed in the methylated analogue of **66**: [Fe$_2$(**L55**)$_3$](ClO$_4$)$_2$ (**69**). The dehydrated complex **69** showed complete [HS–HS] to [LS–LS] switching, upon cooling from 300 K with $T_{1/2}$ = 140 K. Complex **69** also showed complete LIESST mediated [LS–LS] to [HS–HS] switching at low-temperature. The hydrated complex —[Fe$_2$(L$_{55}$)$_3$](ClO$_4$)$_2$·4H$_2$O (**69·4H$_2$O**)—showed a half complete [HS–HS] to [HS–LS] SCO.[103]

High temperature hysteretic SCO in triazole-based dinuclear double-helicate complexes—[Fe$_2$(L$_{56}$)$_3$](PF$_6$)$_2$·5H$_2$O·CH$_3$CN (**70**) and [Fe$_2$(L$_{57}$)$_3$](ASF$_6$)$_2$·3H$_2$O·CH$_3$CN (**71**)—was reported. Complex **70** showed stable two-step SCO behaviour upon repeated cycling. The first gradual SCO step is observed until 432 K followed by the second abrupt step with $T_{1/2}$ = 432 K and ΔT = 11 K at a scan rate of 1 K min^{-1}.[104] The structurally analogous complex **71** (Fig. 12(c)) showed an unsymmetrical and hysteretic [LS–LS] → [HS–HS] SCO in the first heat cool-cycle; $T_{1/2}$ = 443 K and ΔT = 82 K (Fig. 12(d)) were observed at a scan rate of 0.5 K min^{-1}. Subsequent scanning resulted in the modification of the SCO behaviour due to lattice solvent loss. A heterochiral crystal lattice is observed for both the complexes, and the molecular organization in the lattice is governed by π–π and C–H⋯π interactions in **70** and by π–π interactions in **71**. Such intermolecular interactions promoted hysteretic SCO profiles in **70** and **71**. The ΔT = 82 K reported for **71** is the widest hysteresis loop reported so far for a dinuclear-helicate as claimed by the authors of the original study.[18]

A range of tetranuclear tetrahedral cages, tetranuclear [2 × 2] grids, and octanuclear iron(II) complexes based on Schiff base ligands were reported.[45,46] SCO in these systems is gradual most probably due to the lack of cooperativity associated with the intra cage/grid iron(II) switching centres placed

in a slightly different crystallographic environment as observed in dinuclear complex **64**. Due to the lack of abrupt and hysteretic SCO in the multinuclear complexes, a further discussion on them is not presented in this perspective. The interested reader may consult recent reviews by Kruger and co-workers[45] and Brooker and co-workers[46] for more details on the SCO behaviour of multinuclear iron(II) complexes.

3.2. 1D-complexes

A series of 1D-coordination polymers composed of equatorially coordinated tetradentate Jäger-type ligands and axially coordinated ditopic-bidentate ligands such as 4,4′-azopyridine (azpy) (Chart 9) were reported by Weber and co-workers. The nature of self-organization of 1D-chain like architectures, flexibility of the axial ligands, and presence or absence of lattice solvent(s) governed the nature of SCO in 1D-coordination polymers.[57] A few prominent examples showing bistable, abrupt, or stepwise SCO behaviour are detailed as follows.

Complexes $[Fe(L1)(azpy)]_n$ (**72**) and $[Fe(L2)(azpy)]_n$ (**73**) showed two-step SCO (**72**: $T_{1/2}^1 = 326$ K and $T_{1/2}^2 = 156$ K; **73**: $T_{1/2}^1 = 365$ K and $T_{1/2}^2 = 214$ K) with intermediate plateaus comprising equal proportions of LS and HS states; the second switching step of **72** involves a 7 K thermal hysteresis loop. The widths of the intermediate plateaus were estimated to be 110 K and 75 K for **72** and **73**, respectively.

The toluene solvated complex **72·tol** showed gradual one-step SCO with $T_{1/2} = 222$ K. Heating **72·tol** above 390 K led to the loss of the solvent, and the solvent free complex showed two-step SCO like **72** with $T_{1/2}^1 = 320$ K and $T_{1/2}^2 = 150$ K. X-ray structure analysis of **72** at 200 K (plateau region) revealed a layered arrangement. In each layer, a parallel arrangement of 1D-chain like architectures composed of alternating HS and HS iron(II) centres was observed. The layers are interlocked perpendicular to each other leading to a crosslinked arrangement, which caused stepwise SCO in **72** by promoting the formation of an intermediate plateau.[105] A similar hysteretic stepwise

SCO behaviour with an intermediate LS/HS plateau region was reported for $[Fe(L5)(bpea)]_n$ (**74**), $[Fe(L5)(bpea)]_n·0.25MeOH$ (**75**) $[Fe(L5)(bppa)]_n·MeOH$ (**76**), $[Fe(L1)(bipy)]_n·MeOH$ (**77**),[106] and $[Fe(L1)(bpey)]_n$ (**78**).[107] X-ray structure analysis of complexes **74–78** revealed the formation of 1D-chains with linear (bipy), steplike (bpea), and zigzag (bppa) organization. While zigzag chains supported stepwise transitions, stiffness of the axial ligands and number of intermolecular contacts (see below) governed the size of the hysteresis width. Remarkably, $[Fe(L1)(bpea)]·MeOH$ (**79**) showed stable one-step bi-stable SCO ($T_{1/2} = 169$ K and $\Delta T = 27$ K) due to the step like organization of the 1D-chains.[106]

A complete and incomplete cooperative SCO was reported for $[Fe(L3)(bppa)]_n$ (**80**) and $[Fe(L4)(bimm)]_n$ (**81**), respectively. Upon cooling, **81** underwent a gradual SCO from the HS state until 180 K (30% conversion). Further cooling resulted in abrupt spin-state switching of the HS/LS (70 : 30) mixture with $T_{1/2} = 174$ K and $\Delta T = 5$ K. The incomplete SCO observed for **81** is accompanied by a 4 K ($T_{1/2\downarrow} = 136$ K and $T_{1/2\uparrow} = 140$ K) thermal hysteresis loop; below 150 K, a mixed spin-state plateau with $\chi_M T = 1.58$ cm^3 K mol^{-1} was observed. X-ray structure analyses of **80** revealed an increased number of short intermolecular contacts in the abrupt SCO region compared to the gradual region: the role of short intermolecular contacts in causing gradual to abrupt SCO was demonstrated. On the other hand, a zigzag molecular organization was observed in the X-ray structure of **81**. Although such an organization favours stepwise SCO as discussed above, the spin-state switching from the mixed intermediate state to LS state is prohibited in **81** due to restraining interactions associated with the zigzag arrangement.[108]

To get insight into the role of extended aromatic systems in promoting cooperative spin-state switching, a series of iron(II) complexes based on **L6**, **L7**, and **L58** were synthesized. Complexes $[Fe(L6)(bpea)]·MeOH$ (**82·MeOH**) and $[Fe(L6)(bpee)]·MeOH$ (**83·MeOH**) showed abrupt and hysteretic SCO; $T_{1/2} = 209$ K (**82·MeOH**), 230 K (**83·MeOH**) and $\Delta T = 28$ K (**82·MeOH**), and 40 K (**83·MeOH**) were observed. Annealing the complexes at 400 K produced solvent-free complexes **82** and **83**, and the de-solvated complexes showed stable and hysteretic SCO with reduced ΔT relative to their solvated counterparts. Complex $[Fe(L7)(bpee)]$ (**84**) showed abrupt SCO with $T_{1/2} = 149$ K.[109]

The 1D-coordination polymer $[Fe(L58)(bipy)]$ (**85**) shown in Fig. 13(a) underwent stable and above room temperature bi-stable SCO. In the first heat-cool cycle, the complex showed SCO with $T_{1/2} = 352$ K and $\Delta T = 57$ K. A reduced hysteresis width ($\Delta T = 48$ K) and switching temperature ($T_{1/2} = 347$ K) were observed in the second heat-cool cycle; no changes in the SCO behaviour were observed in the subsequent scans (Fig. 13(b)). The SCO is in concert with structural phase transition as revealed by the variable temperature powder X-ray diffraction and differential scanning calorimetry studies. Variable temperature photoluminescence studies evidenced spin-state dependent evolution of PL peaks located at 550 nm and 673 nm (Fig. 13(c)). The intensity of the 550 nm peak
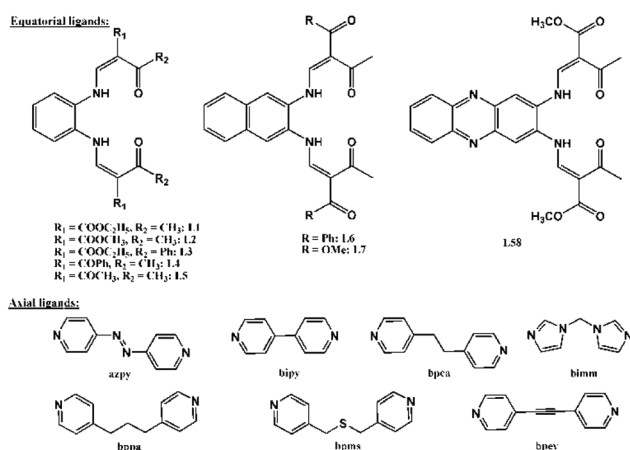
Chart 9 Structures of N$_2$O$_2^{2-}$ equatorially coordinating and ditopic bidentate axially coordinating ligands used to prepare iron(II) 1D-coordination polymers.
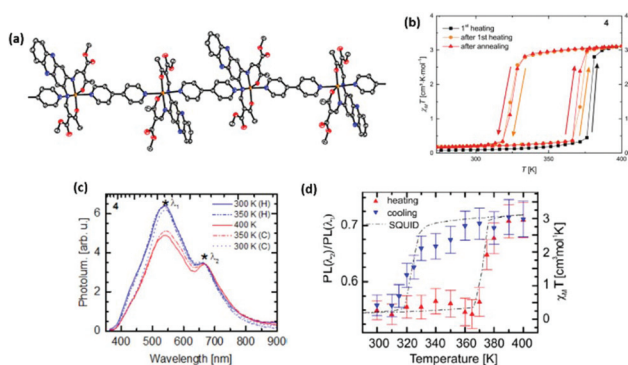
Fig. 13 (a) Representation of the 1D-organization of **85**, (b) $\chi_M T$ versus *T* plots of **85**, (c) temperature dependence of PL intensity of **85** and (d) overlay of $\chi_M T$ versus *T* plot and PL intensity ratio *versus T* plot showing the luminescence read-out of the spin-state of **85**.

decreased with increasing temperature in the 300 K to 400 K range, whereas the intensity of the 673 nm peak varied only slightly with respect to temperature. A plot of the intensity ratio of 550 nm and 673 nm peaks at many temperature points produced a profile like the one obtained from temperature dependent magnetic measurements (Fig. 13(d)). Thus, the luminescence readout of SCO in **85** is demonstrated.[58]

4.   Conclusions

This perspective summarizes various classes of structurally characterized SCO-active mono-, multi-nuclear and 1D-polymeric iron(II)-Schiff base complexes. Some of the complexes showed SCO around RT with or without hysteresis. The SCO properties of the complexes are tuned by varying the precipitation temperature, tailoring a ligand with an appropriate chemical substituent, varying the counter-anion, and employing different solvents of crystallization. However, custom tuning of the SCO properties remains as a big challenge. Although most of the iron(II)-SCO compounds reported in the literature have an all nitrogen (N6) coordination environment, many examples of iron(II)-Schiff base complexes covered in this perspective feature N_4O_2 coordination. Remarkably, some of the N_4O_2-type complexes exhibited abrupt and hysteretic SCO suitable for device applications. The SCO properties of mixed ligand iron(II)-Schiff base complexes are also presented, and the complexes showed spin-state switching characteristics, promising toward device applications. On the other hand, the facile synthesis of functional Schiff base ligands facilitated the selective synthesis of SCO active enantiomeric iron(II) complexes and luminescence read-out of spin-states.

Majority of the SCO complexes presented in this perspective are mononuclear complexes. The realization of abrupt and hysteretic SCO in multi-nuclear iron(II) complexes remains a difficult problem to be tackled. Emphasis should be on obtaining multi-nuclear SCO active iron(II)-Schiff base complexes as

these complexes may bring in cooperative effects causing wide hysteresis loops suitable for potential application purposes.

Conflicts of interest

The authors declare no conflicts of interest regarding the publication of this paper.

Acknowledgements

References

1 P. Gutlich and H. A. Goodwin, in *Spin Crossover in Transition Metal Compounds I*, ed. H. A. Gutlich and P. Goodwin, Springer-Verlag, Berlin, Heidelberg, New York, 2004, pp. 1–47.

2 M. A. Halcrow, *Spin-Crossover Materials Properties and Applications*, John Wiley & Sons, Ltd., Chichester, 2013.

3 S. Brooker, *Chem. Soc. Rev.*, 2015, **44**, 2880–2892.

4 P. Gütlich, Y. Garcia and H. A. Goodwin, *Chem. Soc. Rev.*, 2000, **29**, 419–427.

5 A. Bousseksou, G. Molnár, L. Salmon and W. Nicolazzi, *Chem. Soc. Rev.*, 2011, **40**, 3313–3335.

6 O. Kahn, *Molecular Magnetism*, VCH Publishers, Inc., New York, 1993.

7 K. S. Murray and C. J. Kepert, in *Spin Crossover in Transition Metal Compounds I*, ed. P. Gütlich and H. A. Goodwin, Springer-Verlag, Berlin, Heidelberg, 2004, pp. 195–228.

8 K. Senthil and M. Ruben, *Coord. Chem. Rev.*, 2017, **346**, 176–205.

9 M. M. Khusniyarov, *Chem. – Eur. J.*, 2016, **22**, 15178–15191.

10 S. Venkataramani, U. Jana, M. Dommaschk, F. D. Sönnichsen, F. Tuczek and R. Herges, *Science*, 2011, **331**, 445–448.

11 I. Salitros, N. T. Madhu, R. Boca, J. Pavlik and M. Ruben, *Monatsh. Chem.*, 2009, **140**, 695–733.

12 M. A. Halcrow, *Chem. Lett.*, 2014, **43**, 1178–1188.

13 M. A. Halcrow, *Chem. Commun.*, 2013, **49**, 10890.

14 *Spin crossover in transition metal compounds*, ed. P. Gütlich and H. A. Goodwin, Springer, Berlin, New York, 2004.

15 W. Nicolazzi and A. Bousseksou, *C. R. Chim.*, 2018, **21**, 1060–1074.

16 J. Sanchez Costa, *C. R. Chim.*, 2018, **21**, 1121–1132.

17 L. G. Lavrenova and O. G. Shakirova, *Eur. J. Inorg. Chem.*, 2013, **2013**, 670–682.

18 S. Hora and H. Hagiwara, *Inorganics*, 2017, **5**, 49.

19 M. A. Halcrow, *Chem. Soc. Rev.*, 2008, **37**, 278–289.

20 A. Tissot, J.-F. Bardeau, E. Rivière, F. Brisset and M.-L. Boillot, *Dalton Trans.*, 2010, **39**, 7806.

21 S. Decurtins, P. Gütlich, C. P. Köhler, H. Spiering and A. Hauser, *Chem. Phys. Lett.*, 1984, **85**, 1–4.

22 S. Decurtins, P. Gutlich, K. M. Hasselbach, A. Hauser and H. Spiering, *Inorg. Chem.*, 1985, **24**, 2174–2178.

23 W. Zhang and K. J. Gaffney, *Acc. Chem. Res.*, 2015, **48**, 1140–1148.

24 O. Sato, *Acc. Chem. Res.*, 2003, **36**, 692–700.

25 R. Bertoni, M. Cammarata, M. Lorenc, S. F. Matar, J.-F. Létard, H. T. Lemke and E. Collet, *Acc. Chem. Res.*, 2015, **48**, 774–781.

26 H.-Y. Sun, Y.-S. Meng and T. Liu, *Chem. Commun.*, 2019, **55**, 8359–8373.

27 A. Hauser, *Chem. Phys. Lett.*, 1986, **124**, 543–548.

28 G. Chastanet, M. Lorenc, R. Bertoni and C. Desplanches, *C. R. Chim.*, 2018, **21**, 1075–1094.

29 S. P. Vallone, A. N. Tantillo, A. M. dos Santos, J. J. Molaison, R. Kulmaczewski, A. Chapoy, P. Ahmadi, M. A. Halcrow and K. G. Sandeman, *Adv. Mater.*, 2019, **31**, 1807334.

30 A. B. Gaspar, G. Molnár, A. Rotaru and H. J. Shepherd, *C. R. Chim.*, 2018, **21**, 1095–1120.

31 V. Meded, A. Bagrets, K. Fink, R. Chandrasekar, M. Ruben, F. Evers, A. Bernand-Mantel, J. S. Seldenthuis, A. Beukman and H. S. J. Van Der Zant, *Phys. Rev. B: Condens. Matter Mater. Phys.*, 2011, **83**, 245415.

32 T. G. Gopakumar, F. Matino, H. Naggert, A. Bannwarth, F. Tuczek and R. Berndt, *Angew. Chem., Int. Ed.*, 2012, **51**, 6262–6266.

33 A. Hauser, *Adv. Polym. Sci.*, 2004, **233**, 49–58.

34 B. Weber, W. Bauer and J. Obel, *Angew. Chem., Int. Ed.*, 2008, **47**, 10098–10101.

35 E. Coronado, J. R. Galán-Mascarós, M. Monrabal-Capilla, J. García-Martínez and P. Pardo-Ibáñez, *Adv. Mater.*, 2007, **17**, 1359–1361.

36 B. Weber, E. Kaps, J. Weigand, C. Carbonera, J. F. Létard, K. Achterhold and F. G. Parak, *Inorg. Chem.*, 2008, **47**, 487–496.

37 H. Hagiwara, T. Masuda, T. Ohno, M. Suzuki, T. Udagawa and K. I. Murai, *Cryst. Growth Des.*, 2017, **17**, 6006–6019.

38 B. Schäfer, C. Rajnák, O. Fuhr, D. Klar, C. Schmitz-Antoniak, H. Wende and M. Ruben, *Chem. Commun.*, 2013, **49**, 1098.

39 O. Kahn, *Science*, 1998, **279**, 44–48.

40 A. Real, A. B. Gaspar, V. Niel and M. C. Mun, *Coord. Chem. Rev.*, 2003, **236**, 121–141.

41 K. Senthil Kumar, B. Heinrich, S. Vela, E. Moreno-Pineda, C. Bailly and M. Ruben, *Dalton Trans.*, 2019, **48**, 3825–3830.

42 N. T. Madhu, I. Salitros, F. Schramm, S. Klyatskaya, O. Fuhr and M. Ruben, *C. R. Chim.*, 2008, **11**, 1166–1176.

43 M.-L. Boillot and B. Weber, *C. R. Chim.*, 2018, **21**, 1196–1208.

44 K. Senthil Kumar, I. Šalitroš, B. Heinrich, O. Fuhr and M. Ruben, *J. Mater. Chem. C*, 2015, **3**, 11635–11644.

45 H. S. Scott, R. W. Staniland and P. E. Kruger, *Coord. Chem. Rev.*, 2018, **362**, 24–43.

46 R. W. Hogue, S. Singh and S. Brooker, *Chem. Soc. Rev.*, 2018, **47**, 7303–7338.

47 O. Iasco, E. Rivière, R. Guillot, M. Buron-Le Cointe, J.-F. Meunier, A. Bousseksou and M.-L. Boillot, *Inorg. Chem.*, 2015, **54**, 1791–1799.

48 M. A. Fik, M. Löffler, M. Weselski, M. Kubicki, M. J. Korabik and V. Patroniak, *Polyhedron*, 2015, **102**, 609–614.

49 W. Qin, S. Long, M. Panunzio and S. Biondi, *Molecules*, 2013, **18**, 12264–12289.

50 J. Long, *Front. Chem.*, 2019, **7**, 63.

51 M. Rezaeivala and H. Keypour, *Coord. Chem. Rev.*, 2014, **280**, 203–253.

52 X. Yang, R. A. Jones and S. Huang, *Coord. Chem. Rev.*, 2014, **273–274**, 63–75.

53 C. J. Dhanaraj, J. Johnson, J. Joseph and R. S. Joseyphus, *J. Coord. Chem.*, 2013, **66**, 1416–1450.

54 E. L. Gavey and M. Pilkington, *Coord. Chem. Rev.*, 2015, **296**, 125–152.

55 M. A. Neelakantan, M. Esakkiammal, S. S. Mariappan, J. Dharmaraja and T. Jeyakumar, *Indian J. Pharm. Sci.*, 2010, **72**, 216–222.

56 V. K. K. Praneeth, M. R. Ringenberg and T. R. Ward, *Angew. Chem., Int. Ed.*, 2012, **51**, 10228–10234.

57 B. Weber, *Coord. Chem. Rev.*, 2009, **253**, 2432–2449.

58 C. Lochenie, K. Schötz, F. Panzer, H. Kurz, B. Maier, F. Puchtler, S. Agarwal, A. Köhler and B. Weber, *J. Am. Chem. Soc.*, 2018, **140**, 700–709.

59 Y. Garcia, F. Robert, A. D. Naik, G. Zhou, B. Tinant, K. Robeyns, S. Michotte and L. Piraux, *J. Am. Chem. Soc.*, 2011, **133**, 15850–15853.

60 J. Weihermüller, S. Schlamp, W. Milius, F. Puchtler, J. Breu, P. Ramming, S. Hüttner, S. Agarwal, C. Göbel, M. Hund, G. Papastavrou and B. Weber, *J. Mater. Chem. C*, 2019, **7**, 1151–1163.

61 M. Seredyuk, M. C. Muñoz, M. Castro, T. Romero-Morcillo, A. B. Gaspar and J. A. Real, *Chem. – Eur. J.*, 2013, **19**, 6591–6596.

62 B. Weber, W. Bauer, T. Pfaffeneder, M. M. Dîrtu, A. D. Naik, A. Rotaru and Y. Garcia, *Eur. J. Inorg. Chem.*, 2011, **2011**, 3193–3206.

63 C. Lochenie, W. Bauer, S. Schlamp, P. Thoma and B. Weber, *Z. Anorg. Allg. Chem.*, 2012, **638**, 98–102.

64 C. Lochenie, J. Heinz, W. Milius and B. Weber, *Dalton Trans.*, 2015, **44**, 18065–18077.

65 S. Schlamp, K. Dankhoff and B. Weber, *New J. Chem.*, 2014, **38**, 1965–1972.

66 S. Schlamp, P. Thoma and B. Weber, *Eur. J. Inorg. Chem.*, 2012, **2012**, 2759–2768.

67 J. Weihermüller, S. Schlamp, B. Dittrich and B. Weber, *Inorg. Chem.*, 2019, **58**, 1278–1289.

68 W. Phonsri, D. S. Macedo, K. R. Vignesh, G. Rajaraman, C. G. Davies, G. N. L. Jameson, B. Moubaraki, J. S. Ward,

P. E. Kruger, G. Chastanet and K. S. Murray, *Chem. – Eur. J.*, 2017, **23**, 7052–7065.

69 W. Phonsri, C. G. Davies, G. N. L. Jameson, B. Moubaraki, J. S. Ward, P. E. Kruger, G. Chastanet and K. S. Murray, *Chem. Commun.*, 2017, **53**, 1374–1377.

70 T. Kuroda-Sowa, K. Kimura, J. Kawasaki, T. Okubo and M. Maekawa, *Polyhedron*, 2011, **30**, 3189–3192.

71 L. Zhang, G.-C. Xu, H.-B. Xu, T. Zhang, Z.-M. Wang, M. Yuan and S. Gao, *Chem. Commun.*, 2010, **46**, 2554.

72 K. S. Kumar, M. Studniarek, B. Heinrich, J. Arabski, G. Schmerber, M. Bowen, S. Boukari, E. Beaurepaire, J. Dreiser and M. Ruben, *Adv. Mater.*, 2018, **30**, 1705416.

73 T. Fujigaya, D.-L. Jiang and T. Aida, *J. Am. Chem. Soc.*, 2003, **125**, 14690–14691.

74 A. B. Gaspar and M. Seredyuk, *Coord. Chem. Rev.*, 2014, **268**, 41–58.

75 D. Rosario-Amorin, P. Dechambenoit, A. Bentaleb, M. Rouzières, C. Mathonière and R. Clérac, *J. Am. Chem. Soc.*, 2018, **140**, 98–101.

76 X.-Q. Chen, Y.-D. Cai, W. Jiang, G. Peng, J.-K. Fang, J.-L. Liu, M.-L. Tong and X. Bao, *Inorg. Chem.*, 2019, **58**, 999–1002.

77 L. Zhang, J.-J. Wang, G.-C. Xu, J. Li, D.-Z. Jia and S. Gao, *Dalton Trans.*, 2013, **42**, 8205.

78 B. Benaicha, K. Van Do, A. Yangui, N. Pittala, A. Lusson, M. Sy, G. Bouchez, H. Fourati, C. J. Gómez-García, S. Triki and K. Boukheddaden, *Chem. Sci.*, 2019, **10**, 6791–6798.

79 J.-Y. Ge, Z. Chen, L. Zhang, X. Liang, J. Su, M. Kurmoo and J.-L. Zuo, *Angew. Chem., Int. Ed.*, 2019, **58**, 8789–8793.

80 A.-C. Bas, X. Thompson, L. Salmon, C. Thibault, G. Molnár, O. Palamarciuc, L. Routaboul and A. Bousseksou, *Magnetochemistry*, 2019, **5**, 28.

81 J. Yuan, S.-Q. Wu, M.-J. Liu, O. Sato and H.-Z. Kou, *J. Am. Chem. Soc.*, 2018, **140**, 9426–9433.

82 J. Yuan, M.-J. Liu, S.-Q. Wu, X. Zhu, N. Zhang, O. Sato and H.-Z. Kou, *Inorg. Chem. Front.*, 2019, **6**, 1170–1176.

83 T. Fujinami, K. Nishi, N. Matsumoto, S. Iijima, M. A. Halcrow, Y. Sunatsuki and M. Kojima, *Dalton Trans.*, 2011, **40**, 12301.

84 T. Fujinami, K. Nishi, D. Hamada, K. Murakami, N. Matsumoto, S. Iijima, M. Kojima and Y. Sunatsuki, *Inorg. Chem.*, 2015, **54**, 7291–7300.

85 T. Ueno, Y. Ii, T. Fujinami, N. Matsumoto, S. Iijima and Y. Sunatsuki, *Polyhedron*, 2017, **136**, 13–22.

86 K. Nishi, H. Kondo, T. Fujinami, N. Matsumoto, S. Iijima, M. A. Halcrow, Y. Sunatsuki and M. Kojima, *Eur. J. Inorg. Chem.*, 2013, **2013**, 927–933.

87 K. Nishi, S. Arata, N. Matsumoto, S. Iijima, Y. Sunatsuki, H. Ishida and M. Kojima, *Inorg. Chem.*, 2010, **49**, 1517–1523.

88 W.-K. Han, Z.-H. Li, W. Zhu, T. Li, Z. Li, X. Ren and Z.-G. Gu, *Dalton Trans.*, 2017, **46**, 4218–4224.

89 W. Huang, F. Shen, M. Zhang, D. Wu, F. Pan and O. Sato, *Dalton Trans.*, 2016, **45**, 14911–14918.

90 L. F. Qin, C. Y. Pang, W. K. Han, F. L. Zhang, L. Tian, Z. G. Gu, X. Ren and Z. Li, *Dalton Trans.*, 2016, **45**, 7340–7348.

91 W.-K. Han, L.-F. Qin, C.-Y. Pang, C.-K. Cheng, W. Zhu, Z.-H. Li, Z. Li, X. Ren and Z.-G. Gu, *Dalton Trans.*, 2017, **46**, 8004–8008.

92 D. Ren, X. Sun, L. Gu, D. Qiu, Z. Li and Z. Gu, *Inorg. Chem. Commun.*, 2015, **51**, 50–54.

93 T. Hashibe, T. Fujinami, D. Furusho, N. Matsumoto and Y. Sunatsuki, *Inorg. Chim. Acta*, 2011, **375**, 338–342.

94 L.-F. Qin, C.-Y. Pang, W.-K. Han, F.-L. Zhang, L. Tian, Z.-G. Gu, X. Ren and Z. Li, *CrystEngComm*, 2015, **17**, 7956–7963.

95 N. Struch, N. Wagner, G. Schnakenburg, R. Weisbarth, S. Klos, J. Beck and A. Lützen, *Dalton Trans.*, 2016, **45**, 14023–14029.

96 R. Kulmaczewski, O. Cespedes and M. A. Halcrow, *Inorg. Chem.*, 2017, **56**, 3144–3148.

97 H. Hagiwara and S. Okada, *Chem. Commun.*, 2016, **52**, 815–818.

98 H. Hagiwara, R. Minoura, S. Okada and Y. Sunatsuki, *Chem. Lett.*, 2014, **43**, 950–952.

99 D. Aguilà, P. Dechambenoit, M. Rouzières, C. Mathonière and R. Clérac, *Chem. Commun.*, 2017, **53**, 11588–11591.

100 E. Tailleur, M. Marchivie, N. Daro, G. Chastanet and P. Guionneau, *Chem. Commun.*, 2017, **53**, 4763–4766.

101 Y. Sunatsuki, R. Kawamoto, K. Fujita, H. Maruyama, T. Suzuki, H. Ishida, M. Kojima, S. Iijima and N. Matsumoto, *Inorg. Chem.*, 2009, **48**, 8784–8795.

102 A. R. Craze, N. F. Sciortino, M. M. Badbhade, C. J. Kepert, C. E. Marjo and F. Li, *Inorganics*, 2017, **5**, 1–14.

103 D. Pelleteret, R. Clérac, C. Mathonière, E. Harté, W. Schmitt and P. E. Kruger, *Chem. Commun.*, 2009, 221–223.

104 H. Hagiwara, T. Tanaka and S. Hora, *Dalton Trans.*, 2016, **45**, 17132–17140.

105 W. Bauer, T. Pfaffeneder, K. Achterhold and B. Weber, *Eur. J. Inorg. Chem.*, 2011, **2011**, 3183–3192.

106 W. Bauer, W. Scherer, S. Altmannshofer and B. Weber, *Eur. J. Inorg. Chem.*, 2011, **2011**, 2803–2818.

107 K. Dankhoff, C. Lochenie, F. Puchtler and B. Weber, *Eur. J. Inorg. Chem.*, 2016, **2016**, 2136–2143.

108 T. M. Pfaffeneder, S. Thallmair, W. Bauer and B. Weber, *New J. Chem.*, 2011, **35**, 691–700.

109 C. Lochenie, A. Gebauer, O. Klimm, F. Puchtler and B. Weber, *New J. Chem.*, 2016, **40**, 4687–4695.